Roughness maps to determine the optimum process window parameters in face milling

Xabier Lazkano[a], Patxi X. Aristimuño[a], Oihan Aizpuru[b], Pedro J. Arrazola[a],

[a] *Faculty of engineering, Mondragon Unibertsitatea, Mondragon 20500, Spain*
[b] *Zubiola S. Coop., Azkoitia 20720, Spain*

Abstract

Some industrial applications require structured surfaces with high roughness values to ensure their functionality (R_a > 1 µm, R_{max} < 30 µm). In order to obtain these structured surfaces with high roughness values, face milling operation is commonly used in aluminium components employed in the automotive and aeronautical sectors. Polycrystalline diamond insert tools (PCD) are widely used to obtain those structured surfaces. However, one of the major drawbacks of using face milling is that the roughness presents a high variation across the width of cut. Nevertheless, it is possible to mitigate these variations by (i) modifying the micro-geometry of the inserts, (ii) displacing each tooth by small axial amounts from their nominal positions or (iii) varying the feed rate. Frequently, the definition of those parameters is carried out employing trial-and-error strategies, with consequent cost and time penalties. In this research work, roughness maps have been developed as a novel optimisation tool to define the micro-geometry of the PCD inserts, their axial position in the tool and the feed rate, reducing the time to design new cutting tools for face milling. The roughness maps are determined based on roughness indicators calculated from 3D face milled surfaces that are modelled as a split signal in two components: (i) the kinematic movements of the cutting edge and its geometry, and (ii) a novel approach considering the stochastic roughness, which embraces the chip removal process, material defects or vibrations. The model is validated by experimental face milling tests on A-356 aluminium alloy, showing good agreement with experimental results.

Keywords Roughness, Modelling, Milling, Optimisation, Predictive model

1 Introduction

Surface roughness is one of the most common characteristics employed to assess the quality of machined components. Milne et al. [1] defined this parameter as the repetitive or random deviation from the nominal surface that forms the surface's three-dimensional (3D) topology. Together with surface texturing (Coblas et al. [2]), it has been proven to significantly influence aspects such as tribology, fatigue life, corrosion, sealing, adhesive bonding, osseointegration, and optics.

In the majority of industrial applications, surface roughness is required to be as low as possible to obtain an excellent surface finish or improve the performance of the manufactured workpiece. However, there are many other applications where high roughness values are advantageous (R_a > 1 µm, R_{max} < 30 µm). Mainly, these high roughness values are required on automotive industry (spoilers, door modules, seats, bumpers, and door cappings) or aeronautical industry, where higher roughness results in fewer residue adhesions after impacts, as Kok et al. [3] concluded. Moreover, Persson et al. [4] demonstrated that roughness influences the leakage rate in sealing applications, helps viscoelastic energy dissipation in rubber friction and increases adhesive bonds.

In addition, roughness is also necessary for applications such as healthcare, where dental implants require a specific roughness to ensure adhesion between human tissue and implants (dos Santos et al. [5], Elias et al. [6] and Caravaca [7]).

Different manufacturing strategies are used to structure the rough surfaces, including sandblasting (Caravaca [7]), laser (Mumtaz and Hopkinson [8]), grinding (Hecker and Liang [9]), honing (Buj-Corral et al. [10]), and machining (Bernardos and Vosniakos [11]). Machining is most commonly used in the industrial manufacturing sector, owing to its speed and comparatively lower cost. As most of the applications requiring high roughness values belong to the automotive and aeronautical sectors, lightweight alloys are critical to reduce the weight of vehicles and aircrafts. Among the light alloys, aluminium is one of the most widely used, which is usually machined by tools having polycrystalline diamond inserts (PCD).

Among the machining operations, face milling is one of the most commonly used to control surface roughness. However, achieving the required roughness values in this process presents a higher degree of complexity than in other operations. While in turning, surface roughness depends mainly on the nose radius and the feed per turn, in face milling, the surface is generated by several edges whose traces are not constant across the surface. In consequence, highly variable roughness values are obtained across the width of cut.

This fact is further complicated when some applications require a specific roughness range to be functional. Due to the variability of the roughness obtained by face milling, depending on the relative position between the tool and the workpiece to be machined (see Figure 1), it is usually complex to comply with the limits of the range. In addition, roughness variability can lead to an erroneous idea of the actual surface roughness. Single roughness measurements performed with a roughness tester do not give reliable information on the actual distribution of the roughness obtained by face milling. Consequently, cutting conditions may be defined inaccurately and cutting tools may be designed incorrectly.

These difficulties lead to a reliance on trial-and-error strategies for tool design and manufacturing, and the need for additional resources (time, workers, materials, and energy) to correct the tool geometry and the cutting conditions. The trial-and-error strategy is usually based on the company's accumulated experience, and in most cases, this information is neither structured nor collected. Hence, it is challenging to design a tool correctly on the first try. If the customer is flexible with the cutting conditions, there can be a margin of error in the tool design. Otherwise, it is exclusively restricted to the tool geometry. Consequently, launching times could increase up to three weeks.

Given these challenges, several authors investigated the face milling process in an attempt to reduce this economic impact and improve efficiency. Regarding the cutting conditions, Korkut and Donertas [12] and Alauddin et al. [13] concluded that surface roughness increases with the feed rate and decreases with the cutting speed. In a further study, Reddy and Rao [14] determined that feed rate is the most dominant effect for a given tool geometry, and cutting speed the least.

In contrast, when end-milling titanium Ti-6Al-4V Sun et al. [15] observed that roughness increases in the cutting direction at a cutting speed of between 50 and 80 m/min, and decreases above 80 m/min. The same authors found that surface roughness increases almost linearly with the feed rate, but this was disputed by Baek et al. [16], who concluded that it is non-linear due to run-out effects. Regarding the axial depth of cut, Lopez de la Calle et al. [17] reported that it has no influence over the surface roughness, whereas Alauddin et al. [13] concluded the opposite.

Studies were also performed for micro-milling, as Lu et al. [18] concluded that the order of the parameters affecting the roughness is the feed rate, spindle speed, radius of ball-end milling and axial depth of cut.

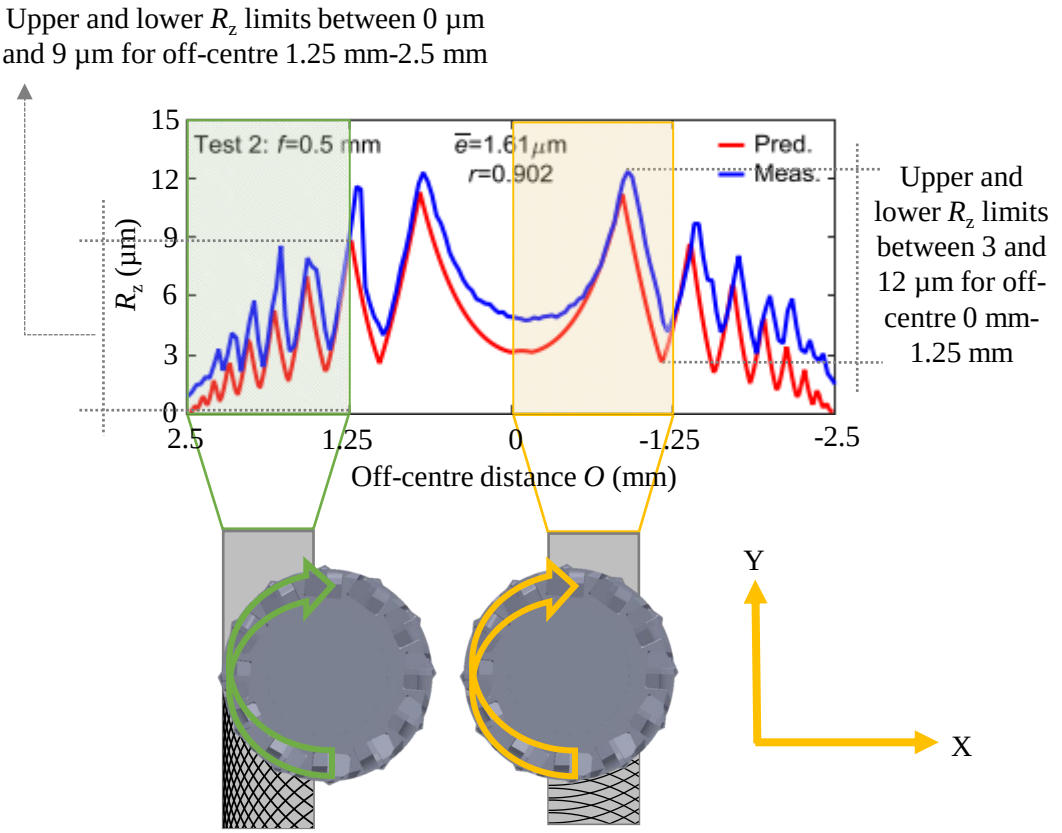

Figure 1. Example of R_z distribution in the cross-feed direction in face milling operation (adapted from [19]). The distribution of roughness indicators is variable in the cross-feed direction, due to tool rotation. Moreover, depending on the relative position between the workpiece and the tool, different roughness values can be achieved without changing cutting conditions and tool geometry.

As regards the geometric parameters of the tool, Reddy and Rao [14] reported that the radial rake angle increases roughness due to a change in the sharpness of the cutting edge, which leads to a change in the cutting edge contact length. The same authors also found that the nose radius influences surface roughness. Moreover, Wang and Chang [20] observed that roughness increases by increasing the axial relief angle and concavity angle, when the concavity angle is more than 2.5°. Baptista and Simoes [21] found that roughness is reduced by tilting the tool in the feed direction. Wang and Chang [20] achieved a similar reduction by applying coolant, as the cutting fluids reduce the frictions between tool and chip/workpiece. However, Ezugwu et al. [22] determined that the coolant pressure does not affect roughness values. As it can be concluded, there is considerable uncertainty in identifying appropriately the behaviour of roughness on face milled surfaces.

Additionally, several authors applied this knowledge to develop surface roughness predictive models with which define efficient and accurate process planning (tool trajectory and cutting conditions) and tool geometries. Surface roughness predictive models analysed in this literature review have been classified in two groups: empirical and kinematic.

Likewise, empirical models are divided in two approaches, Artificial Neural Network (ANN) and experimental. The first ones consist of training an ANN with the roughness results measured from experimental tests. Geometrical parameters of the tool, cutting conditions and workpiece material properties are used as input data, and experimental roughness results as output data. And

experimental approaches examine the effects of cutting parameters like feed rate, depth of cut or cutting speed through the execution of experiments and the analysis of results for developing equations that estimate roughness indicators.

Additionally, kinematic models based on the machining theory to represent machined 2D profiles and 3D surfaces. Mainly based on the geometry of the tool and movements of the cutting edges.

In regard to ANN approaches, Tsai et al. [23] developed a predictive model with four inputs (spindle speed, feed rate, depth of cut, and vibration average per revolution) and one output (R_a roughness indicator). Similarly, Bernardos and Vosniakos [24] predicted R_a parameter in face milling. The input parameters were the feed per tooth, cutting speed, tool-workpiece engagement, tool wear, cutting fluid, and the cutting force's three components. Hossain et al. [25] developed a model that uses the cutting speed, feed rate, and depth of cut as input data. And Liu et al. [26] a model that considers the cutting speed, depth of cut, width of cut and feed rate as input parameters.

Other authors used ANNs together with other types of solutions to predict roughness. Wu and Lei [27] analysed the utility of using the signal features in vibration measurements during the milling process and the cutting parameters to predict the surface roughness. Palani and Natarajan [28] integrated an ANN into a machine vision system in order to predict the roughness of milling operation. Moreover, Kant and Sangwang [29] combined ANN with Genetic Algorithm (GA), Mahesh et al. [30] combined Response Surface Methodology (RSM) for prediction and GA for optimisation and Yeganefar et al. [31] Support Vector Machine (SVM), ANN and regression analysis. Finally, Kadirgama et al. [32] compared RSM, SVM and Potential Support Vector Machine (PSVM), concluding that the most accurate results are obtained with the last one.

Other than to predict, Ozcelik et al. [33] and Oktem et al. [34] used ANN to optimise cutting conditions for minimising surface roughness and Huang et al. [35] to adapt the feed rate to a limit roughness. In addition, Oktem [36] used ANN for adapting the cutting conditions to achieve the desired roughness, Escamilla et al. [37] for optimising cutting speed, feed rate and depth of cut and Malghan et al. [38] for surface roughness, cutting forces and power consumption. Pinar et al. [39] applied neural networks for optimising cooling conditions.

In general, ANN models are more successful when compared to the rest of approaches in terms of speed, simplicity and capacity to learn from examples. There are no required assumptions or hypotheses as in experimental or kinematic models, and the performance of the calculus can be improved by adding more levels for the input parameters. However, as concluded by Zain et al. [40], a high quantity of experimental tests is required for creating a realistic network. Moreover, it is time-consuming for further improvement by defining more levels of input parameters, and the repeatability of the tests is not assured.

Regarding experimental approaches, Tipnis et al. [41] and Alauddin et al. [13] developed equations to predict R_a depending on the cutting speed, feed rate and axial depth of cut. Using a similar approach, Alauddin et al. [42] developed a model for Inconel 718 as a function of the feed rate and cutting speed. Mansour and Abdalla [43] also developed a model for EN32 steel. Recently, Liu et al, [44] combined an analytical calculation of the specific cutting energy consumption (SCEC) and empirical characterization of the relationship between the surface roughness and the SCEC to predict R_a in slot milling. They concluded that R_a is probably a function of SCEC at a given depth of cut. Overall, the drawback of empirical models is that they are only valid for the cutting conditions, tool geometry and workpiece materials used in the experimental tests.

In contrast, Kinematic models are valid for any cutting condition and tool geometry, which makes them more attractive from an industrial point of view. Kinematic models are classified in two groups: (i) the models performing single 2D profile simulations and (ii) the models performing

multiple 2D profile simulations in order to generate 3D rough surfaces. In this last case, the obtained information is more detailed, and a broader view can be taken when designing tools or defining cutting conditions.

Regarding 2D profile simulations, some authors developed models that consider tool run-out, tool geometry and cutting conditions (Baek et al. [16] and Muñoz-Escalona and Maropoulos [45]). Feng et al. [46] proposed a model for lasser-assisted end milling based on the kinematics of tool movement and elastic response of workpiece. In addition, based on these two parameters, Feng et al. [47] developed a model for ultrasonic vibration-assisted milling.

Regarding 3D face milled simulations, several authors proposed approaches to develop the 3D rough surfaces. Ehmann and Hong [48] and Arizmendi et al. [49] developed two models based on the geometry of the tool and the effect of tool vibrations, Zhang et al. [50] considered tool wear and Arizmendi et al. [51] the tool parallel axis offset. Regarding the models to calculate the roughness indicators based on these 3D surfaces, Ryu et al. [52] and Franco et al. [53] developed similar models in which tool deflections, radial and axial run-outs, back-cutting and tool tilting are taken into account. The first authors analysed the distribution of R_a and R_{max} across the width of cut, and determined that these two indicators decrease in the external areas of the width of cut. In addition, they concluded that roughness indicators as R_a and R_{max} are not enough to describe the topography of a surface, and proposed further use of standard deviation, skewness and kurtosis. And the second authors focused on analysing in depth the effect of each of the parameters. Moreover, Buj-Corral et al. [54] analysed the effect of the feed rate, tool eccentricity and helix angle in side milling, proposing a model that considers grinding errors.

Apart from the cutting and geometric parameters, other authors focused additionally on the effects of the cutting process stability and on the material properties. Concerning the process stability, Zhenyu et al. [55] introduced the dynamic characteristics of the milling process in order to consider phenomena as forced vibrations. They also concluded that the axial and radial run-outs have more influence than the feed per tooth. In the same line, Wojciechowski et al. [56] presented a model for cylindrical milling taking into account dynamic phenomena related to instantaneous tool deflections. In addition, Omar et al. [57] developed a model to simultaneously predict conventional cutting forces and 3D surface topography of the axial direction during side milling. The model incorporates the effects of tool run-out, tool deflection, system dynamics, flank face wear, and tool tilting on surface roughness. Finally, Lu et al. [58] considered cutting force and dynamic characteristics to estimate deformations in micro-milling and apply their effect on surface roughness. Regarding the material properties, Lu et al. [59] developed a model for micro-end milling based on the vibrations, tool movement and the forming of workpiece surface governed by elastic recovery and tool geometry. Vibrations were measured through experiments.

More recently, two papers have been presented with important advances in the calculation of 3D rough surfaces. On the one hand, Arizmendi and Jimenez [19] proposed a model in which the 3D face milled surfaces were obtained based on a regularly spaced grid of points defined along the feed and pick feed directions. The developed methodology predicts the surface height at each grid point as a result of the cutting edge trajectories of tool inserts in face milling operations. The model is also capable of calculating the roughness of overlapped face milled surfaces. On the other hand, Urbikain and Lopez de Lacalle [60] developed a model for inclined milling during 5-axis machining using circle-segment end-mills, considering tool geometry, feed rate, radial immersion, and tool run-out.

As it can be concluded, most of the research analysed in the literature review is focused on the influence of cutting conditions, process faults, cutting dynamics and tool deformations. However, and to the best of the author's knowledge, no study has been found which analyses the variation of the axial and radial positions of the inserts in the mill, as well as using inserts with different

micro-geometries mounted in the same tool (nose radii, end-edge angles), or the effect of modifying these micro-geometries. These analyses could be of great interest for automotive and aeronautical sectors, as it would allow to reach and control the high roughness values (R_a > 1 µm, R_{max} < 30 µm) without changing the cutting conditions of the process.

Furthermore, the models analysed in the literature review focus on predicting surface roughness in a specific situation. However, they do not explicitly offer the possibility to optimise the tool geometry or cutting conditions by providing simulation results of a wide range of conditions simultaneously. In fact, the need has been identified to develop a simulation tool that provides a global view of the actual roughness state. By varying certain cutting conditions or geometrical parameters of the tool, this optimisation tool would generally show the actual roughness values. Consequently, the most appropriate parameters to meet the roughness requirements could be successfully chosen at the first attempt. With the use of this new approach, the trial-and-error experimental strategies could be considerably reduced.

Additionally, from the literature review it has been concluded that external factors to the tool geometry and cutting conditions, such as vibrations, workpiece defects or process faults could be important in roughness predictions. These factors would be of particular interest for calculating precisely the roughness indicators that are directly dependent on the peak-to-valley distances of the roughness profile, such as R_z, R_t and R_{max}.

However, other parameters such as the elastic recovery of the workpiece material and the minimum chip thickness are neglected when modelling high roughness values (R_a > 1 µm, R_{max} < 30 µm). As mentioned by Shimada et al. [61] for materials such as aluminium or copper alloys, the minimum chip thickness is 5% of the cutting edge radius. Consequently, for such high roughness indicators, the elastic recovery of the workpiece material and the minimum chip thickness could be considered negligible. In addition, when machining aluminium alloys with PCD inserts, Pattnaik et al. [62] concluded that tool wear was minimum, so could therefore be disregarded for this tool-workpiece couple.

Therefore, in the present paper, a novel approach called roughness maps is proposed as an efficient optimisation strategy to identify the appropriate geometry of the tool and cutting conditions to achieve the desired roughness. To obtain the maps, a predictive model is developed for 3D surface roughness predictions in face milling operation with polycrystalline diamond inserts (PCD). The model is oriented to predict 3D face milled surfaces with high roughness values (R_a > 1 µm, R_{max} < 30 µm). The 3D surfaces are modelled as a split signal in two components: (i) the kinematic movements of the cutting edge and its geometry, and (ii) a novel approach considering the stochastic roughness, which takes into account the chip removal process, material defects, vibrations, etc. In the model, the back-cutting effect, axial and radial run-outs and cutting edge micro-geometry are considered.

The roughness 3D surface is obtained calculating the 2D roughness profiles of the complete width of cut, from which R_a, R_z, R_t and R_{max} indicators are calculated. The model is then experimentally validated for an A-356 aluminium alloy, material widely used in the automotive and aeronautical industries where high roughness values are often required. Additionally, a sensitivity analysis is performed to study the effects of feed rate, teeth quantity, teeth position in the tool, axial and radial position of the teeth and teeth micro-geometry on the roughness.

Nomenclature

A_p	maximum amplitude of the stochastic roughness profile	a_p	depth of cut
C	chord of the teeth trajectory	C_c	correlation coefficient

f_{prop}	proportional feed per turn according to C	f_z	feed per tooth
f_v	feed per turn	$f_{z\ scraper}$	feed per scraper tooth
$f_{z\ limit}$	limit feed rate	dh_t	incremental axial differential distance
h_t	axial differential distance	O	off-centre distance
i	end-edge angle	P_y	y position of the teeth in advance
O_f	offset	P_z	z position of the teeth
P_{ypos}	y position of the teeth in back-cutting	R_a	arithmetic mean roughness
R	tool radius	R_n	nose radius
R_{max}	maximum peak-to-valley height of one cut-off	R_z	mean of the maximum peak-to-valley height of the complete profile
R_t	maximum peak-to-valley height of the complete profile	r	cutting edge radius
r_t	radial differential distance of a tooth	T_s	scraper teeth
T_r	roughing teeth	y	y coordinates of the tooth geometry
V_c	cutting speed	z	z coordinates of the tooth geometry
y_{pos}	y coordinates of the tooth geometry in back-cutting	Z_s	scraper teeth number
Z	number of teeth	α	clearance angle
θ	off-centre angle	γ_a	axial rake angle
γ_r	radial rake angle		

2 Surface roughness predictive model for face milling operation and roughness maps optimization tool

The roughness predictive model developed in this research work focused on face milling. This operation consists on milling flat surfaces perpendicular to the axis of rotation of the cutter. In face milling, the tool is usually displaced perpendicular to its axis so that cutting occurs on the circumference of the cutter. As the mill enters the workpiece, the tool's cutting edges repeatedly cut into and exit from the material, shaving off chips from the workpiece with each pass. The way the material is cut, i.e., the tool is displaced in the feed direction and rotates on its axis (see Figure 2), influences surface roughness generation.

The roughness of face milled workpieces is highly complex. In contrast to other machining operations such as turning, the surface is generated by several cutting edges, and the geometry and position of these greatly influence the roughness surface. For example, when face milling a surface with a width of cut of 25%, the way the tool is positioned in respect to the workpiece will significantly influence the roughness and possibly the cycle time. In fact, due to back-cutting of milling operations, the topography of the surfaces is usually complex, and different roughness values are achieved on the same surface (see Figure 2).

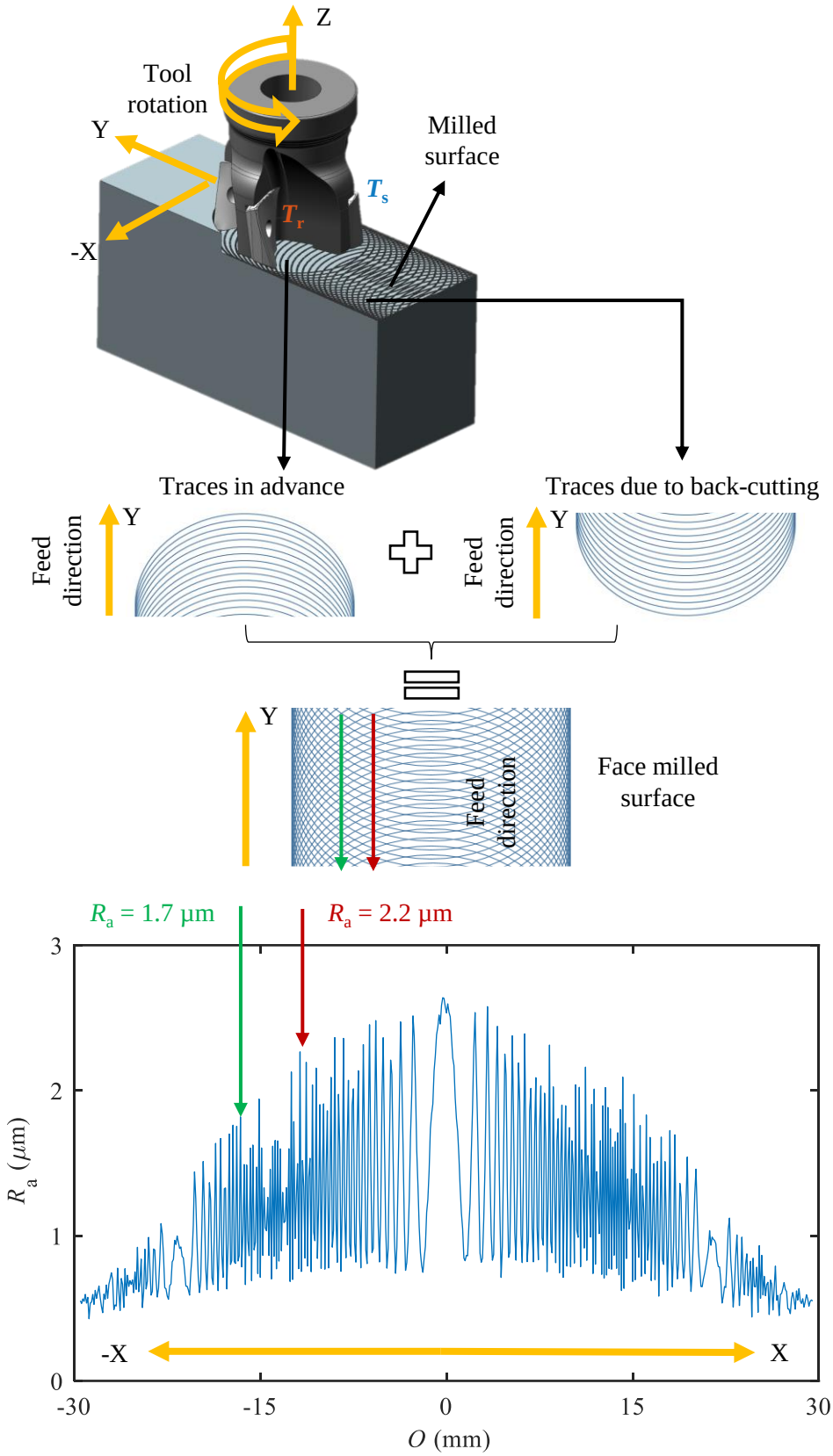

Figure 2. Roughness generation in face milling using scraper (T_s) and roughing teeth (T_r). Due to tool rotation, scraper teeth generate traces in advance and due to back-cutting (marked by blue lines). As observed, the topography of the surface is heterogeneous, so roughness indicators vary in the width of the cut (R_a is shown as an example).

In industrial applications, one of the options for structuring a surface by face milling is to use teeth with different geometries, frequently using two types of inserts: roughing teeth and scraper

teeth. The roughing inserts (T_r in Figure 2) have a near wiper geometry, which carry out a function close to plateau honing. They have a minor end-edge angle i (3º) and produce a small theoretical peak-to-valley height. The scraper inserts (T_s in Figure 2) have a grooving action. Having a nose radius at a lower axial position than the roughing inserts, it generates valleys in the nearly flat surface created by the wiper edges.

In milling, the roughness profile can be divided into the primary geometric profile, secondary geometric profile (both corresponding to the kinematics of the cutting operation) and stochastic profile. The primary geometric profile is created by the teeth in advance (red coloured profile in Figure 3 a)), and the secondary geometric profile by the traces generated by the same teeth due to back-cutting (blue coloured profile in Figure 3 a)). Both profiles form the kinematic roughness profile. Then, the stochastic roughness profile corresponds to the effect of the chip removal process, material defects or vibrations, and in general corresponds to a profile of lower amplitude than the one generated by the kinematics of the cutting process (see Figure 3 b)). Finally, once being able to accurately model rough surfaces, roughness maps are developed as an optimization tool that provides the optimum cutting conditions and tool geometry faster than performing individual simulations.

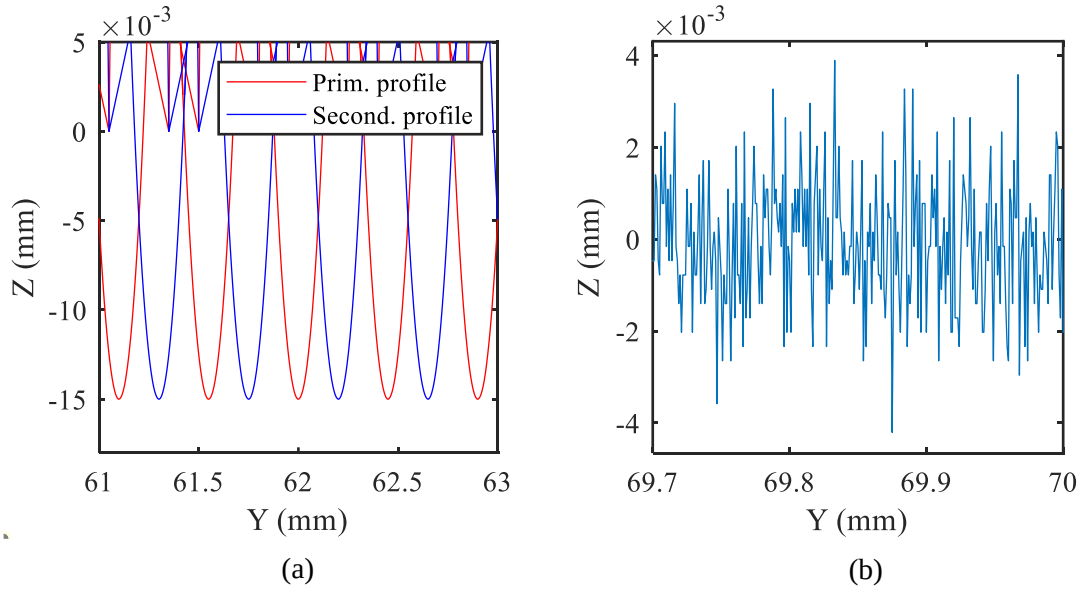

Figure 3. a) Example of the primary (in red) and the secondary (in blue) geometric roughness profiles, b) Example of a stochastic roughness profile.

2.1 Modelling of the kinematic roughness

In order to model the kinematic component of the roughness profile, it is necessary to define the micro-geometry of the scraper and roughing teeth that compose the face mill cutter. For this purpose, the value of the different radii and edges that compose each tooth are first defined in the model. Consequently, vectors containing the coordinates defining the outline of the scraper and roughing teeth are generated. A graphical description of the definition of the insert geometries is described in Figure 31 in the appendix.

Once defined the microgeometry of the scraper and roughing teeth, the model calculates the traces left by each tooth during one cutting turn. For this purpose, the radial position of each tooth in the tool ($R_j\cos(\theta)$) and their corresponding feed per tooth (f_z) are added on the one hand to the feed direction coordinates defining the contours of the teeth y_j, as shown in Figure 4 a) and b),

Equations (1) and (2) and Figure 5 a). In this manner, each tooth contour is placed in its corresponding position in the feed direction of the cutting (P_y distance in Y direction).

On the other hand, each contour is placed in its corresponding P_z distance (axial position, Z direction), adding the corresponding axial differential distance h_t (see Figure 4 c)) to the Z coordinates of the teeth contours z_j, as in Equation (3). In this manner, the coordinates of the traces left by each tooth in advance are defined.

$$\theta = \sin^{-1}\left(\frac{O}{R_j}\right) \tag{1}$$

$$P_{yj} = y_j + R_j \cos(\theta) + jf_z \tag{2}$$

$$P_{zj} = z_j + h_t \tag{3}$$

where j is the number of teeth in study. However, in face milling, the teeth also generate traces in the surface due to back-cutting, and their geometry is symmetrical to that of the traces generated in advance with Equations (2) and (3) (see Figure 5 a)).

In order to determine first their position in the feed direction, the chord C of the trajectory performed by each tooth during the cutting turn is estimated with Equation (4), considering the off-centre distance at which the roughness calculation is being performed. The proportional part of the feed per turn (f_{prop}) that the tool has advanced in this period must then be calculated as in Equation (5), where f_v is the feed per turn. And finally, to calculate the position of each trace in the back-cutting P_{ypos}, C and f_{prop} distances are subtracted from P_y, as in Equation (6).

$$C = 2R_j \cos(\theta) \tag{4}$$

$$f_{prop} = f_v \frac{(180 + 2\theta)}{360} \tag{5}$$

$$P_{yposj} = P_{yj} - C - f_{prop} \tag{6}$$

Moreover, the geometry of the back-cutting traces is obtained by multiplying the Y coordinates of the traces in advance by -1, as in Equation (7). In this manner, the contour of the traces left by the teeth in advance (primary geometric profile) and due to back-cutting (secondary geometric profile) are obtained, as shown in Figure 5 a) and b).

$$y_{posj} = -1 \cdot y_j \tag{7}$$

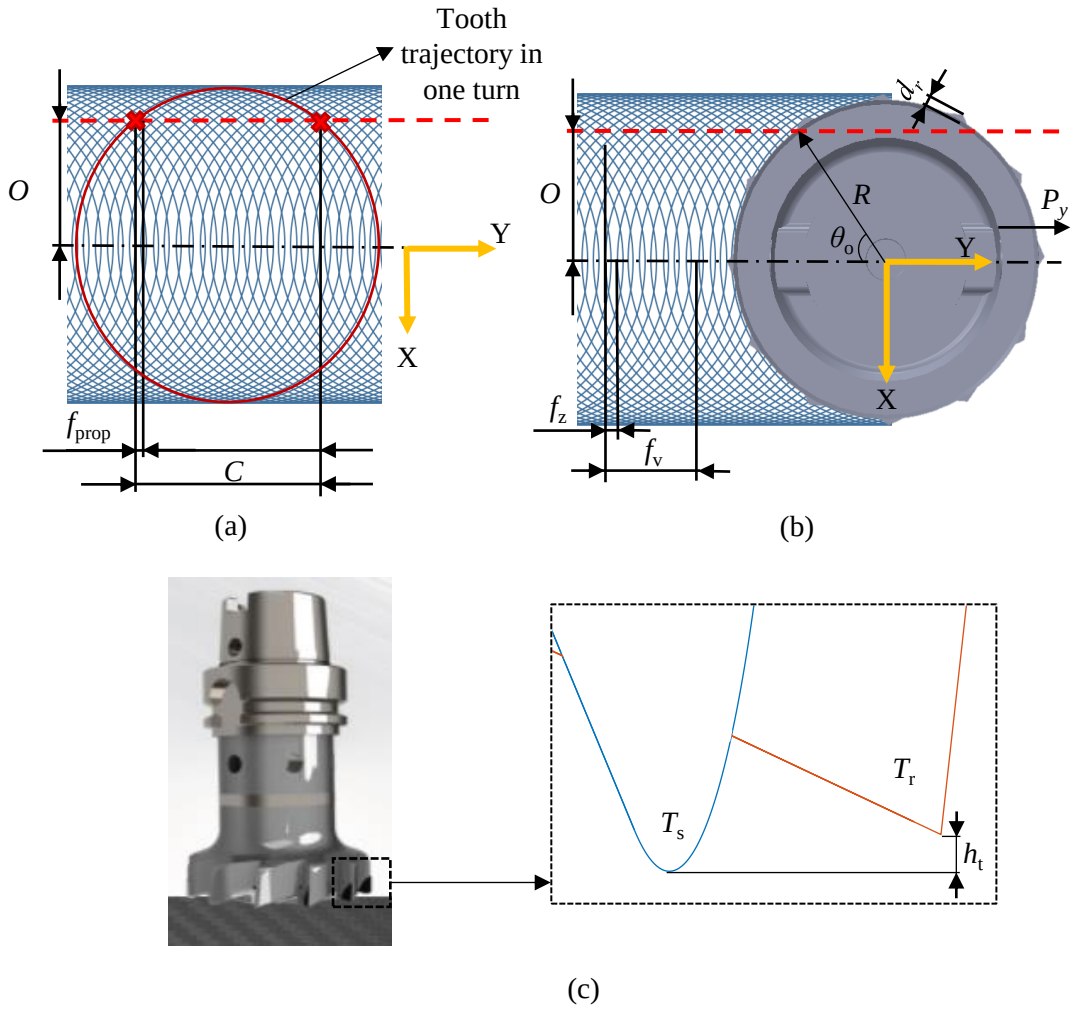

Figure 4. Variables for insert position definition in the model, a) and b) top view. The tooth trajectory is marked in solid red, and the off-centre distance in discontinuous red. The mill advances in Y direction. c) axial differential distance between T_r and T_s.

Then, the process is repeated for as many cutting turns as necessary to comply with the cut-off distance. The cut-off is the length of the reference line used to separate the irregularities forming the surface roughness. To evaluate the roughness profile, five cut-offs are required, and the length of each cut-off depends on the value of R_a.

And finally, the intersection points between the traces left by the teeth in advance (primary geometric profile) and due to back-cutting (secondary geometric profile) are calculated (see Figure 5 c). For this purpose, vertical lines are drawn over the primary and secondary geometric profiles every 5 μm of distance. And then, all the coordinates of these geometric profiles that intersect with these vertical lines are identified, keeping the values of the intersection occurring at a lower height. In this way, the parts of the traces left by the teeth that are in contact with the workpiece are identified, obtaining the kinematic roughness profile (see Figure 5 d)).

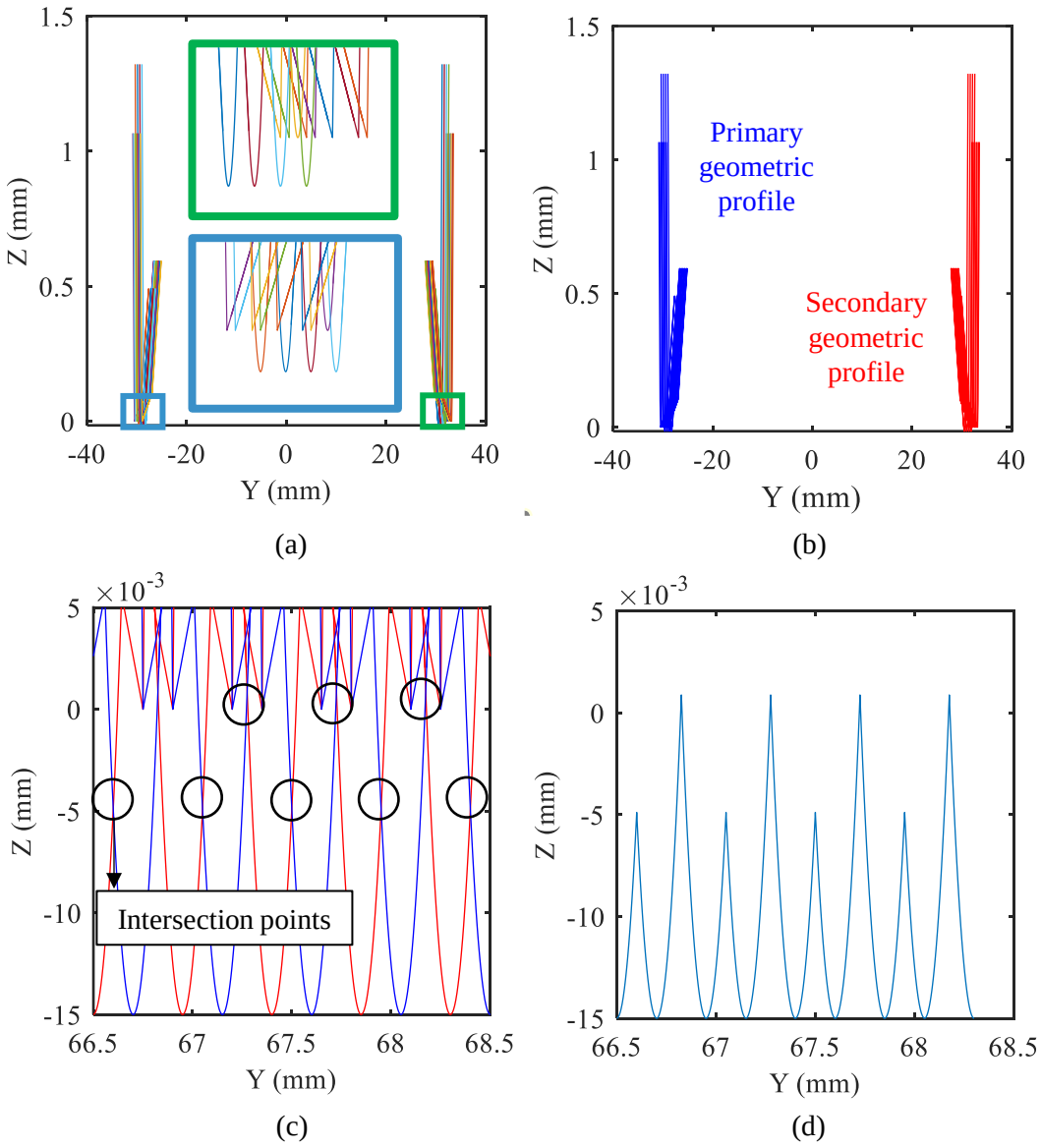

Figure 5. Generation of the kinematic roughness profile in face milling at f_z 0.15 mm/z: a) traces left by the teeth in one turn, b) primary and secondary geometric roughness profiles after one turn, c) zoom over the primary and secondary geometric roughness profiles after several turns, and d) kinematic roughness profile after calculating the intersection points.

2.2 Modelling of the stochastic roughness

In contrast to the kinematic component of roughness, the modelling of the stochastic part was based on experimentally measured face milling roughness profiles. The experimental set-up and the cutting conditions are explained in section 3.

After performing the face milling experimental tests, roughness profiles were measured at different off-centre distances (0 mm, 10 mm and 20 mm) with Alicona IFG4 profilometer (see Figure 6 a)). Then, with Matlab software, a high pass filter was applied to each profile in order to eliminate the experimental kinematic part of the roughness (effect of the teeth geometry and movements of the cutting edge) and obtain the experimental stochastic roughness (see Figure 6 b)). The frequency value of the filter was defined in function of the topography of each roughness

profile. The maximum amplitude (A_p) of each of the stochastic profiles (maximum peak-to-valley distance) was then estimated.

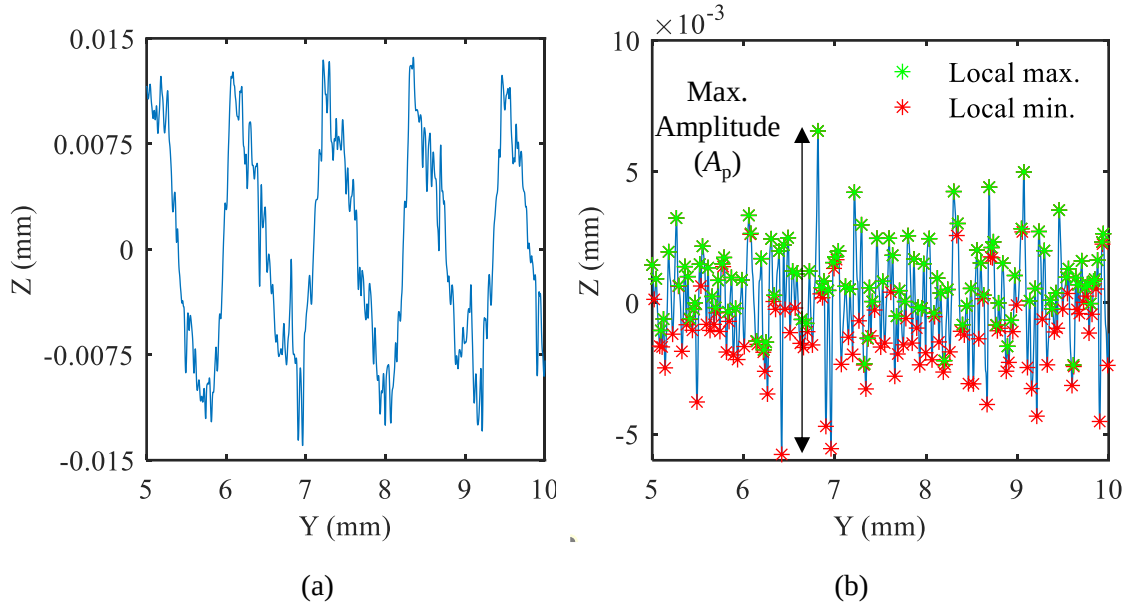

Figure 6. Process of obtaining the experimental stochastic roughness profiles, a) An experimentally measured roughness profile, b) Stochastic roughness profile after high pass filtering. The maximum amplitude of the stochastic roughness profile and the local maxima (green asterisks) and minima (red asterisks) are also shown.

Analysing the value of all the estimated A_p in respect to the cutting conditions, it was observed that a higher cutting speed (see Figure 32 a)) and the use of lubrication (flood milling, see Figure 32 c)) reduced its value. In contrast, a higher depth of cut increased A_p (see Figure 32 b)), while no influence was perceived when using MQL for this material and cutting conditions (see Figure 32 d)). Moreover, it was observed that a higher feed rate increases the roughness values. This can be observed in of the appendix.

Hence, three equations were developed to estimate A_p, one for each lubricant condition: dry (8), flood (9), and MQL (10), which are shown in Table 1. R-square indicator showed accurate correlation (90.91%) for the three equations.

Table 1. Equations for calculating the maximum amplitude of the stochastic roughness profiles in function of the feed rate, cutting speed and depth of cut. R-square statistical indicator is also shown for each equation.

Lubrication	Equation	R^2 (%)	
Dry	$A_p = 0.0096 + 0.028f_z - 0.000004V_c + 0.001671a_p$		(8)
Flood	$A_p = 0.0083 + 0.028f_z - 0.000004V_c + 0.001671a_p$	90.91	(9)
MQL	$A_p = 0.00972 + 0.028f_z - 0.000004V_c + 0.001671a_p$		(10)

In addition, the local maxima and minima of all the experimental stochastic roughness profiles were identified and classified in 35 groups according to their Z-axis values (height). Hence, the number of local maxima and minima classified in each group was calculated, and thus estimate the frequency with which they appear in the experimental stochastic roughness profiles.

Identifying these frequency appearances enabled the modelling of more realistic stochastic roughness profiles. In fact, the highest peaks and deepest valleys appear less frequently (0.5%), and the ones of smaller amplitude are more likely to appear. The frequency appearances are shown in Figure 33 of the appendix.

Therefore, in order to obtain the modelled stochastic roughness profile, its maximum amplitude is first calculated via Matlab software using Equations (8), (9) or (10) and the cutting conditions. Then, a vector with random Z-axis coordinates is generated with 'Randsample' command considering the calculated maximum amplitude and the appearance frequencies, obtaining the modelled stochastic roughness profile. Finally, this profile is added to the kinematic roughness profile (see Figure 7 a) and b)).

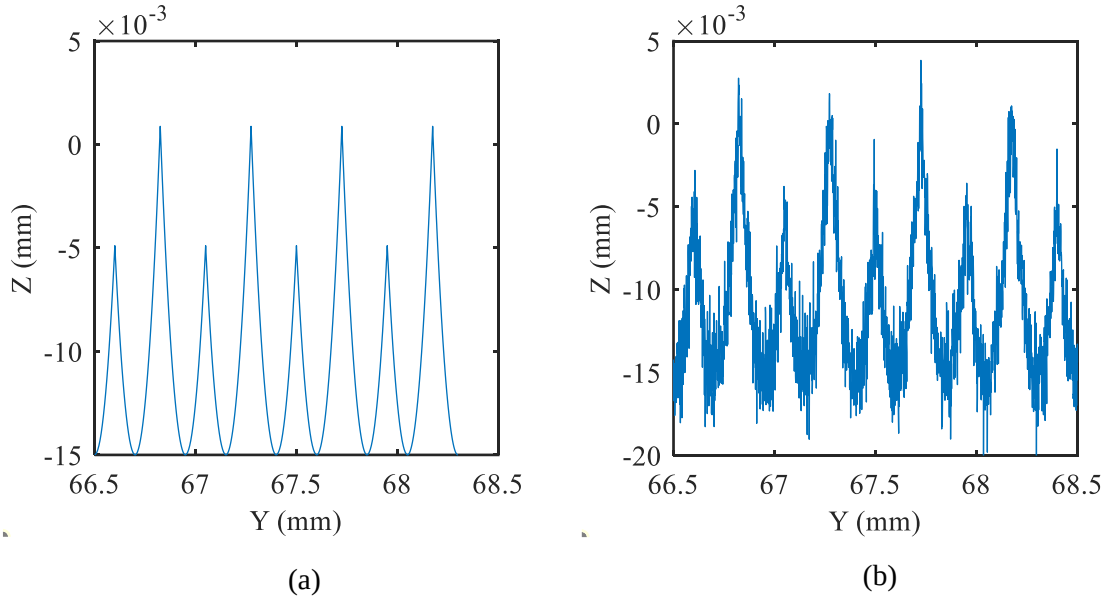

Figure 7. Example of how it is obtained the modelled roughness profile at f_z 0.15 mm/z, a) Kinematic roughness profile and b) Roughness profile (kinematic roughness profile with stochastic roughness).

Since the equations developed to estimate stochastic roughness have been obtained from face milling tests, they are not considered projectable to other machining operations. However, to apply the stochastic roughness in another machining operation, the procedure developed in this subsection could be followed based on experimental tests carried out for that cutting operation.

The whole process of calculating the kinematic and stochastic part of the roughness profiles is repeated for all the off-centre distances defined in the width of cut of the tool. And this process is summarized in the flow chart of Figure 34 in the appendix.

2.3 Roughness maps

After being able to predict the roughness considering the kinematic and the stochastic part of the roughness profiles, the model was adapted to predict the roughness maps. This optimisation tool determines the percentage of the width of cut that comply with the required roughness indicators, being helpful for toolmakers in tool design.

As demonstrated throughout this paper, obtaining specific roughness values by face milling is challenging, due to the variable behaviour of the roughness in the entire width of cut. Due to this variability, it is likely to obtain areas where the roughness does not comply with the requirements of the manufacturing process.

However, using the roughness maps, it is possible to know what percentage of the face milled surface will achieve the roughness requirements of the manufacturing process. By offering a comprehensive view of the roughness obtained across the width of cut, roughness maps permit achieving the roughness requirements while the productivity and the tool life are maximised Currently, the process of adjusting the tool geometry and cutting conditions is mainly performed by experimental trial-and-error strategies, with the high economic cost that this entails. However, trial-and-error are strategies are considerably reduced applying this novel concept.

Before carrying out the simulation, there are defined most of the geometrical parameters of the tool and the cutting conditions, except the feed rate (f_z), nose radius of the scraper teeth (R_n) and axial differential distance (h_t). Between these three parameters, one is fixed and a set of simulations is performed by varying the other two parameters within a range (depending on the number of calculi selected for each variable, between 100 and 200 simulations providing results for roughness distributions could be presented). Consequently, the model calculates the roughness indicators for the entire range of study.

Next, the upper and lower limits of the roughness indicators are defined. Hence, it is possible to calculate what percentage of the roughness indicators calculated with the model comply with the established limits. Finally, these percentages are displayed in function of the two variables selected for the simulation, obtaining the maps. The yellow areas of the maps show the combination of parameters (f_z, R_n or h_t) that best meet the requirements of the manufacturing process (higher percentage). In contrast, the blue areas show those with the lowest percentage.

If the requirements of the manufacturing process claim the modification of other parameter than the relative height between teeth, the nose radius or the feed per tooth, it is necessary to simulate new roughness maps, which lasts 12 hours approximately.

In this research work, one example is going to be shown for each combination, (i) feed rate and the axial differential distance, (ii) feed rate and the nose radius of scraper teeth and (iii) axial differential distance and the nose radius of the scraper teeth. For the simulations, the tool described at the beginning of chapter 5 was used.

Using the map relating the feed rate and the axial differential distance permits optimising the manufacturing process. In fact, this kind of map helps determining the maximum f_z without compromising the roughness limits, and thus reduce production times. In addition, allows identifying the appropriate axial differential distance between the scraper and roughing teeth to meet the requirements of the manufacturing process once the feed rate has been maximised.

In Figure 8, a map for a f_z range of 0.05-0.2 mm/z and a dh_t between 0-0.015 mm is shown, being the default value of h_t 0.015 mm (h_t range 0.015-0.03 mm). The percentages shown in the maps correspond to a limit for R_a between 5-25 µm and R_{max} < 30 µm. The map illustrates how the zone with the highest percentage complying with the roughness requirements (marked in yellow as a 93%) corresponds to a feed rate between 0.12-0.15 mm/z and a relative height increase of 0 and 0.005 mm (h_t of 0.015-0.02 mm). If production was to be maximised, an f_z of 0.15 mm/z and dh_t of 0 mm (h_t 0.015 mm) would be chosen. Moreover, it can be observed that the roughness requirements are met with a dh_t from 0 mm to 0.005 mm (h_t 0.015 mm to 0.02 mm) for f_z 0.13 mm/z.

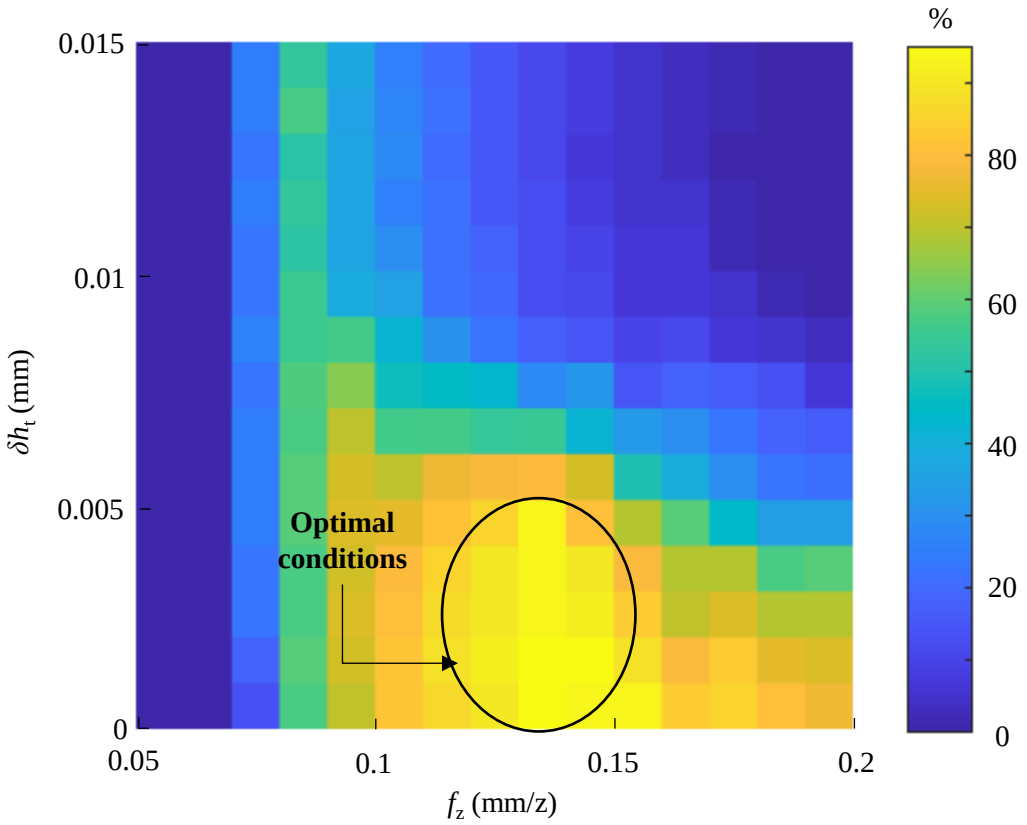

Figure 8. Example of a roughness map in function of h_t and f_z. Yellow zones are the conditions with the highest percentage complying with the roughness requirements (optimal conditions), whereas the blue zones are the ones with lowest percentage.

Using the map relating the feed rate and the nose radius of scraper teeth, the manufacturing process and the tool geometry can be optimised. On the one hand, allows finding the maximum possible feed rate with which also meet the roughness requirements. Simultaneously, allows the design of inserts with the maximum possible nose radius, to avoid excessive wear and increase the tool life.

For example, a map for a f_z range of 0.05-0.2 mm/z and a nose radius 0.1-1.1 mm is presented in Figure 9. The percentage values shown in the map correspond to a limit for R_a between 5-25 µm and R_{max} < 30 µm. The map displays two zones in which the percentage of achieving the roughness requirements are higher (marked in yellow as a 93%), (i) at f_z 0.07-0.1 mm/z and R_n 0.1-0.3 mm and (ii) at f_z 0.12-0.14 mm/z and R_n 0.4- 0.7 mm.

In this case, an f_z of 0.14 mm/z and R_n of 0.7 mm would be chosen. In this manner, it would be possible to work with the maximum possible f_z and R_n to maximise production, minimise tool wear effect and meet the requirements of the manufacturing process.

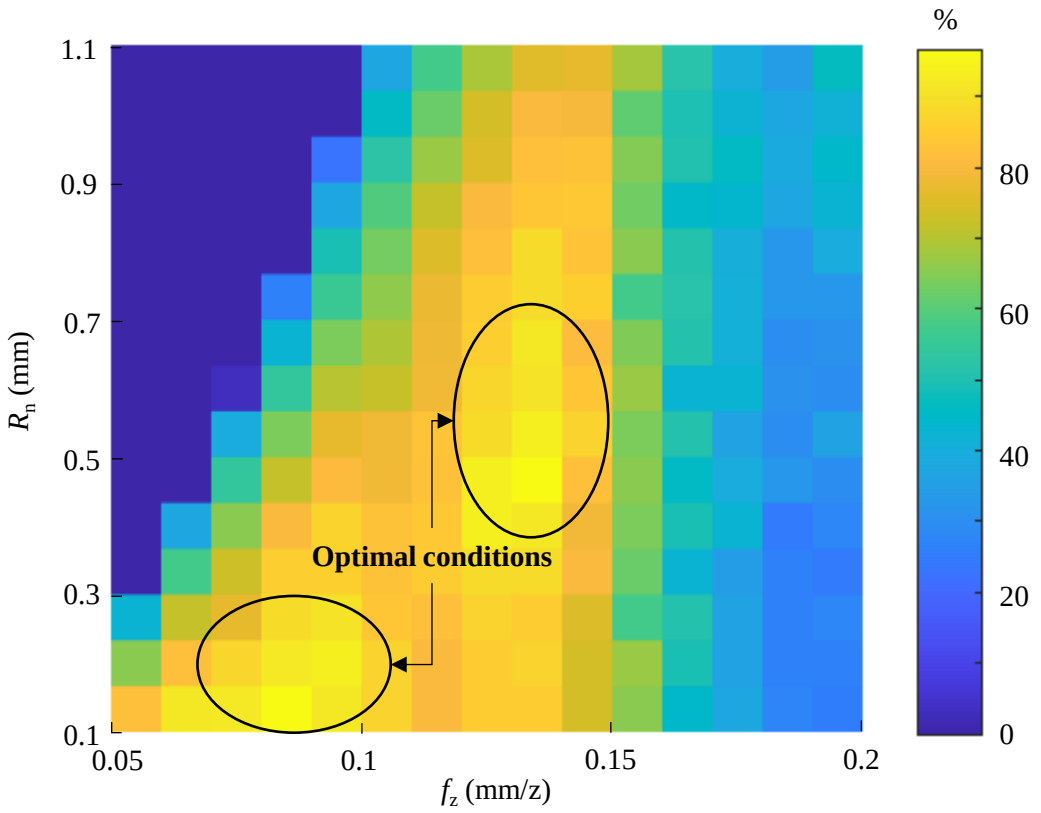

Figure 9. Example of a roughness map as a function of R_n, and f_z. Yellow zones are the conditions with the highest percentage complying with the roughness requirements (optimal conditions), whereas the blue zones are the ones with lowest percentage. In this case, two different zones are considered as optimum.

Finally, the map relating the axial differential distance and the nose radius of the scraper teeth allows optimising the tool geometry. As the cutting conditions remain constant, it allows finding the optimum tool geometry to meet the roughness requirements. Hence, the maximum possible nose radius can be identified to avoid excessive tool wear, and the axial differential distance can be adjusted to meet the customer's requirements.

For example, Figure 10 shows a map for a R_n of 0.1-1.1 mm and a $\mathrm{d}h_t$ of 0-0.015 mm, being the default value of h_t 0.015 mm (h_t range of 0.015-0.03 mm). The reported percentage values correspond to a limit for R_a between 10-25 µm and R_{max} < 40 µm. The map features a single zone where the percentage of achieving the roughness requirements is higher (marked in yellow as an 85%), at $\mathrm{d}h_t$ 0.007-0.01 mm (h_t 0.022-0.025 mm) and R_n of 0.2-0.5 mm. In order to minimise tool wear effect, the maximum R_n would be chosen (0.5 mm), and the corresponding $\mathrm{d}h_t$ would be 0.01 mm (h_t 0.025 mm).

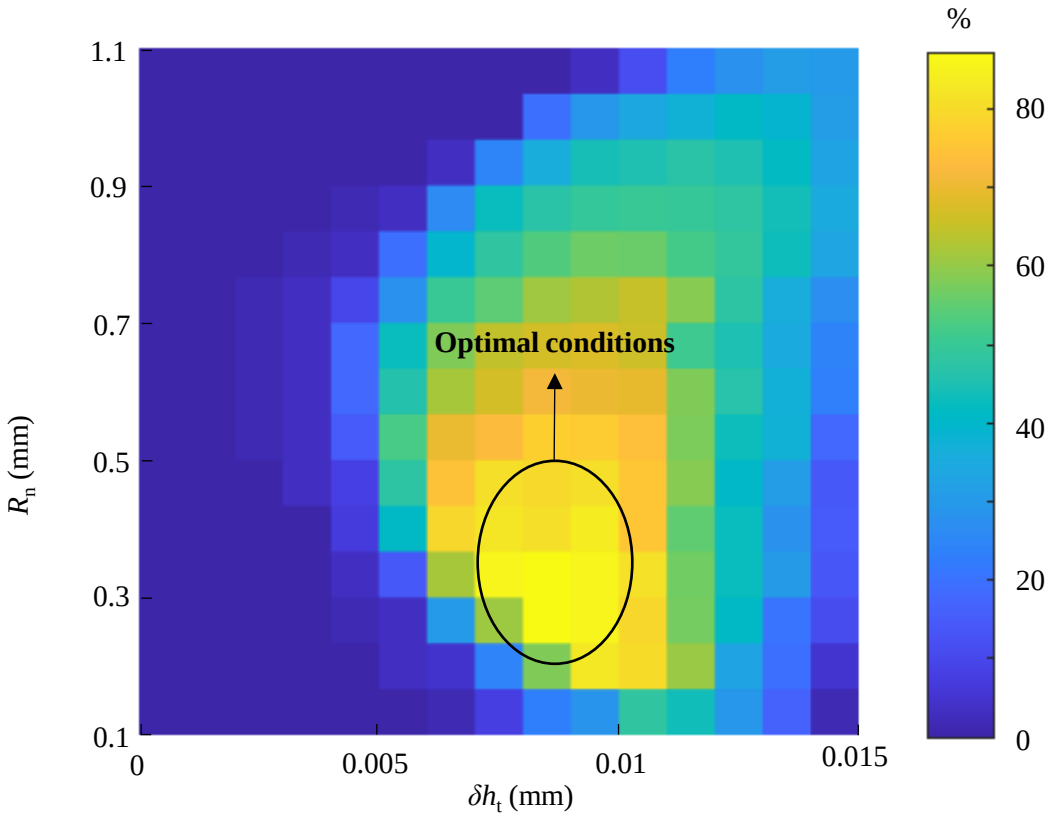

Figure 10. Example of a roughness map as a function of R_n and h_t. The yellow zones are the conditions with the highest percentage complying with the roughness requirements (optimal conditions), whereas the blue zones are the ones with lowest percentage.

3 Experimental tests

In order to validate the predictive model and estimate the stochastic component of the roughness profile, experimental face milling tests were performed in a GF Mikron MILL P 800 U 5 axis machine using a 12 teeth mill with polycrystalline diamond inserts (PCD) of CBT010 grade fabricated by Zubiola S. Coop. The scraper teeth are located at a diameter of 61 mm at positions 1-4-7-10 in the cutting tool (out of 12 teeth), whereas the roughing teeth are placed at a diameter of 63 mm at positions 2-3-5-6-8-9-11-12 (see Figure 11 a)). The scraper teeth are positioned 15 µm axially below the roughing teeth. The nose radius of the scraper teeth is 0.5 mm, and the end-edge angle of the roughing teeth is 3º.

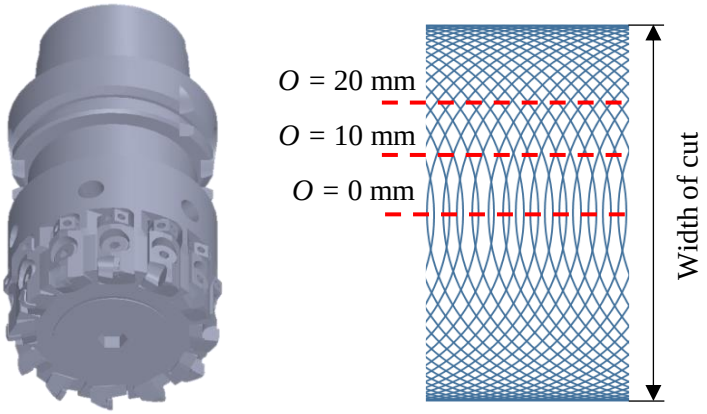

Figure 11. a) Mill used in the experimental tests, b) Marks left on the surface (blue coloured). The dashed red lines indicate the O values at which roughness measurements have been performed.

Each tooth's effective axial and radial differential positions were estimated from the 3D surfaces measured in Alicona IFG4 profilometer (see Table 2). Axial differential distance (h_t) values are measured in reference to the roughing tooth placed at the highest height on the tool (teeth number 5 in Table 2), considering its axial height to be 0 mm. The radial differential position r_t is measured with regard to the nominal radius of each tooth. The errors in the estimation of the teeth positions were approximately of 2 µm. These axial and radial differential positions are related to the difficulty of positioning each tooth in its nominal position.

Table 2. Axial (h_t) and radial (r_t) differential positions of each tooth (T_s) = scraper, (T_r) = roughing. h_t is measured taking tooth number 5 as a reference. r_t is measured considering as a reference the nominal radius of each tooth.

Teeth number	1 (T_s)	2 (T_r)	3 (T_r)	4 (T_s)	5 (T_r)	6 (T_r)	7 (T_s)	8 (T_r)	9 (T_r)	10 (T_s)	11 (T_r)	12 (T_r)
h_t (µm)	-16	-3	-3	-14	0	-1	-13	-4	-5	-16	-24	-3
r_t (µm)	60	0	0	60	0	0	60	0	0	0	0	0

The experimental tests involved face milling an A-356 aluminium alloy workpiece off 75x100 mm at the cutting conditions detailed in Table 3. Roughness measurements were carried out at 0 mm, 10 mm, and 20 mm from the centre of the trajectory of the tool (off-centre distance), as shown in Figure 11 b). For each test, two repetitions were performed. Roughness measurements were carried out in an Alicona IFG4 profilometer using a 10x objective lens.

Table 3. Cutting conditions for face milling experimental tests. Each test has been assigned a number (test number), which is valid for the three O distances (0 mm, 10 mm and 20 mm).

γ_r (º)	γ_a (º)	α (º)	Teeth distribution	r	Coolant	a_p (mm)	V_c (m/min)	f_z (mm/z), (test number)
5	3	10	2 T_r per 1 T_s	3.7	No	1	1000	0.01 (1), 0.04 (2), 0.1 (3), 0.2 (4)
5	3	10	2 T_r per 1 T_s	3.7	No	1	800	0.01 (5), 0.04 (6), 0.1 (7), 0.2(8)
5	3	10	2 T_r per 1 T_s	3.7	No	1	1200	0.01 (9), 0.04 (10), 0.1 (11), 0.2 (12)
5	3	10	2 T_r per 1 T_s	3.7	Flood	1	1000	0.01 (13), 0.04 (14), 0.1 (15), 0.2 (16)
5	3	10	2 T_r per 1 T_s	3.7	MQL	1	1000	0.01 (17), 0.04 (18), 0.1 (19), 0.2 (20)
5	3	10	2 T_r per 1 T_s	3.7	No	2	1000	0.01 (21), 0.04 (22), 0.1 (23), 0.2 (24)
0	3	10	1 T_r per 1 T_s	3.7	No	1	1000	0.01 (25), 0.04 (26), 0.1 (27), 0.15 (28), 0.2 (29)

4 Model validation

The predictive model was validated in two manners. On the one hand, a comparison of the roughness indicators (R_a, R_z, R_t, R_{max}) obtained from the experimental measurements and the model at O 0 mm, 10 mm and 20 mm (see subsection 4.1). On the other hand, a comparison of the 2D roughness profiles and 3D roughness surfaces obtained from experimental measurements and the model (see subsection 4.2). In this research work, the validation of the roughness profiles and surfaces is shown for test numbers 1, 2, 3 and 4.

4.1 Comparison of experimental and modelled roughness indicators

Regarding the modelled and experimentally obtained roughness indicators, Table 4 shows their average, maximum and minimum values at O = 0 mm, O = 10 mm and O = 20 mm. As it can be observed, high roughness values were induced over the workpieces. The measurement uncertainty of the experimental indicators was estimated at 6%, performing two measurements. Detailed prediction errors for each indicator and test number are shown in the appendix (Figure 35 for O = 0 mm, Figure 36 for O = 10 mm and Figure 37 for O = 20 mm).

Table 4. Average, maximum and minimum values of the experimentally measured and modelled roughness indicators (R_a, R_{max}, R_t, and R_z), at O 0 mm, 10 mm and 20 mm for the 29 test numbers.

	O = 0 mm		O = 10 mm		O = 20 mm	
	Experimental	Modelled	Experimental	Modelled	Experimental	Modelled
R_a (μm)	$3.8^{+3.7}_{-2.5}$	$3.8^{+3.7}_{-2.1}$	$3.6^{+3.6}_{-2.4}$	$3.4^{+4.8}_{-2.3}$	$3^{+2.6}_{-2.2}$	$3.1^{+3.5}_{-1.8}$
R_{max} (μm)	$22.8^{+17}_{-13.9}$	$23^{+18.1}_{-13.9}$	$20.6^{+15.8}_{-13.6}$	$21.8^{+22.8}_{-14.3}$	$17.2^{+12}_{-12.3}$	$19.9^{+17.5}_{-11.8}$
R_t (μm)	$23.4^{+17.4}_{-14.2}$	$23.7^{+18.2}_{-14.8}$	$21.2^{+16.4}_{-14}$	$22.2^{+22.4}_{-14.2}$	$17.9^{+12.7}_{-12.6}$	$20.6^{+16.8}_{-12.1}$
R_z (μm)	$21.8^{+15.9}_{-13.1}$	$21.8^{+18.5}_{-13.9}$	$19.9^{+15.9}_{-12.9}$	$20.4^{+22.4}_{-13.6}$	$16.7^{+12.}_{-11.9}$	$18.7^{+15.8}_{-11.}$

In order to estimate the contribution of the stochastic roughness, average errors were calculated implementing the stochastic roughness ('S' column) and not implementing it ('NS' column), thus only considering the kinematic roughness (see Table 5). In addition, the improvement percentage of the predictions was also calculated when applying stochastic roughness ('Improv.').

It should be noted that the response of the equations estimating the stochastic roughness is aleatory due to the use of 'Randsample' Matlab command. Although Equations (8), (9) and (10) depend on the cutting conditions, the topography of the stochastic roughness profile changes from simulation to simulation. Nevertheless, it was estimated that this random response varies the results by 4% for the same cutting conditions and tool geometry.

Table 5. Average errors taking into account the stochastic roughness ('S' column) and not taking into account the stochastic roughness ('NS' column). In addition, the improvement percentage obtained applying the stochastic roughness is shown in 'Improv.' column. Average errors are shown for O 0 mm, 10 mm and 20 mm.

Average errors	O = 0 mm			O = 10 mm			O = 20 mm		
	S (μm)	NS (μm)	Improv. %	S (μm)	NS (μm)	Improv.%	S (μm)	NS (μm)	Improv %
R_a	0.53	0.82	36	0.45	0.68	34	0.42	0.45	7
R_{max}	1.73	6.83	75	2.67	5.39	50	2.95	4.04	27
R_t	2.06	7.03	71	2.52	5.74	56	3.08	4.47	31
R_z	1.51	6.44	76	1.97	5.24	62	2.37	4.01	41

As it can be observed in 'S' column, average errors considering the stochastic roughness were between 0.42-0.53 μm for R_a, 1.73-2.95 μm for R_{max}, 2.06-3.08 μm for R_t and 1.51-2.37 μm for R_z, which were considered accurate. Moreover, it can be observed how avoiding the stochastic roughness, the average errors considerably increased (see Table 5 'NS' column). The most significant improvements occurred in the indicators that depend directly on the peak-to-valley distance (R_{max}, R_t and R_x, see Table 5 'Improv. %' column). These improvements occurred because the stochastic roughness increases the value of the peaks and valleys, achieving roughness profiles closer to those measured experimentally. For these reasons, it was concluded that the stochastic roughness is necessary for predicting accurately the surface roughness in face milling.

Nevertheless, it is possible to achieve the same roughness indicators with completely different roughness profiles. For this reason, the roughness 2D profiles and 3D surfaces were also validated.

4.2 Comparison of experimental and modelled roughness 2D profiles and 3D surfaces

To complement the validation performed with the roughness indicators, an additional validation was performed by comparing 2D roughness profiles and 3D roughness surfaces. Overall, it was concluded that the profiles as well as the surfaces were geometrically close to those experimentally measured. In the four cases shown in Figure 12 (test number 1), Figure 13 (test number 2), Figure 14 (test number 3) and Figure 15 (test number 4), the traces left by the roughing tooth at -24 μm can be observed, to the point where it dominates the profile at test number 1 (0.01 mm/z) and test number 2 (0.04 mm/z). As the feed rate increases, the valleys and peaks become more separated from each other, which means that the roughing tooth at -24 μm removes fewer peaks and valleys created by adjacent teeth and thus does not fully master the profile topography.

Moreover, the amplitude of the 2D roughness profiles is greater at higher feed rates. This occurs because increasing the feed rate causes the peaks and valleys to be generated at a greater distance from each other. Consequently, the intersections between the traces occur at greater heights, causing deeper valleys and higher peaks. For example, at test number 1 the maximum amplitude is about 7.6 μm (see Figure 12 c), whereas at test number 4 is about 25.7 μm (see Figure 15 c).

It can be observed that the main differences are related to the height of the peaks and valleys. The cause could lie in the following three factors. On the one hand, built-up edge might lead to an enlargement of the height of the teeth, generating more profound valleys on the surface. On the other hand, an error in the estimation of the height at which the inserts are fixed could rise to these

differences. In fact, placing the teeth at the appropriate height is a laborious task in which positioning errors can occur. Finally, side flow could deform the peaks, varying their height and geometry.

Nevertheless, considering the stochastic roughness more realistic profiles were achieved, as the adjacent peaks and valleys do not show the repeatability that they show in the kinematic profile (see Figure 7 a)).

In order to quantify the accuracy of the 2D profiles, the correlation coefficients C_c were calculated. In general, the modelled profiles showed a good lineal positive correlation with the experimental ones, higher than 0.8. Table 6 shows the C_c for the four cases studied in this subsection.

Table 6. Coefficients of correlation for the 2D roughness profiles of test number 1, 2, 3 and 4.

	C_c
Test number 1	0.86
Test number 2	0.85
Test number 3	0.91
Test number 4	0.87

Concerning the 3D roughness surfaces, it can be seen that the highest peaks and lowest valleys are mainly located at the central zone of the tool trajectory, and moving away from this area, they diminish. It can also be noticed that increasing the feed rate increases the peak-to-valley distance, generating rougher surfaces.

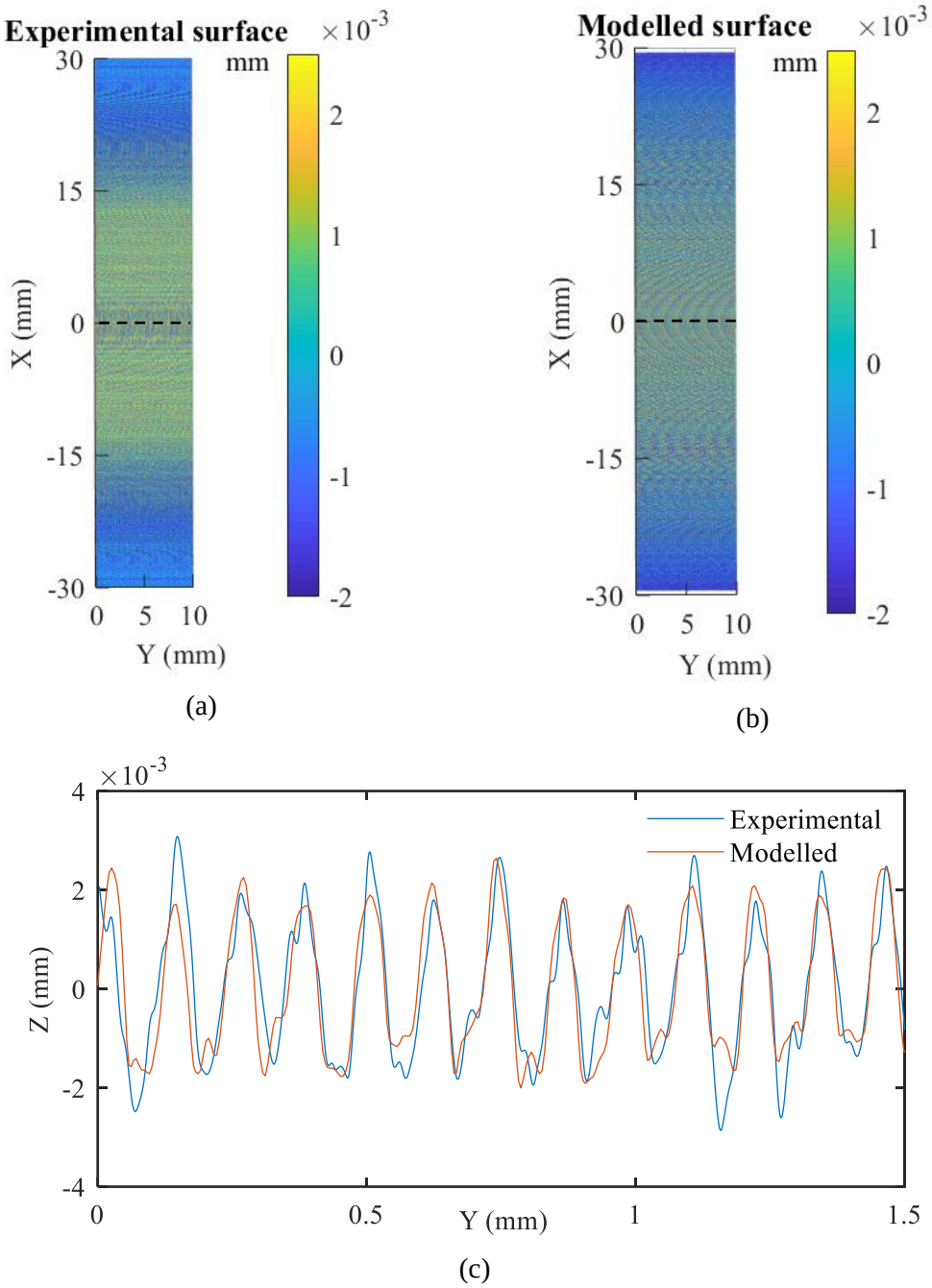

Figure 12. Comparison of experimental and modelled 2D and 3D profiles for test number 1. The black dashed line over the rough surfaces indicates the O at which the 2D roughness profile was obtained (at 0 mm), a) Experimental surface, b) Modelled surface, c) Profile comparison.

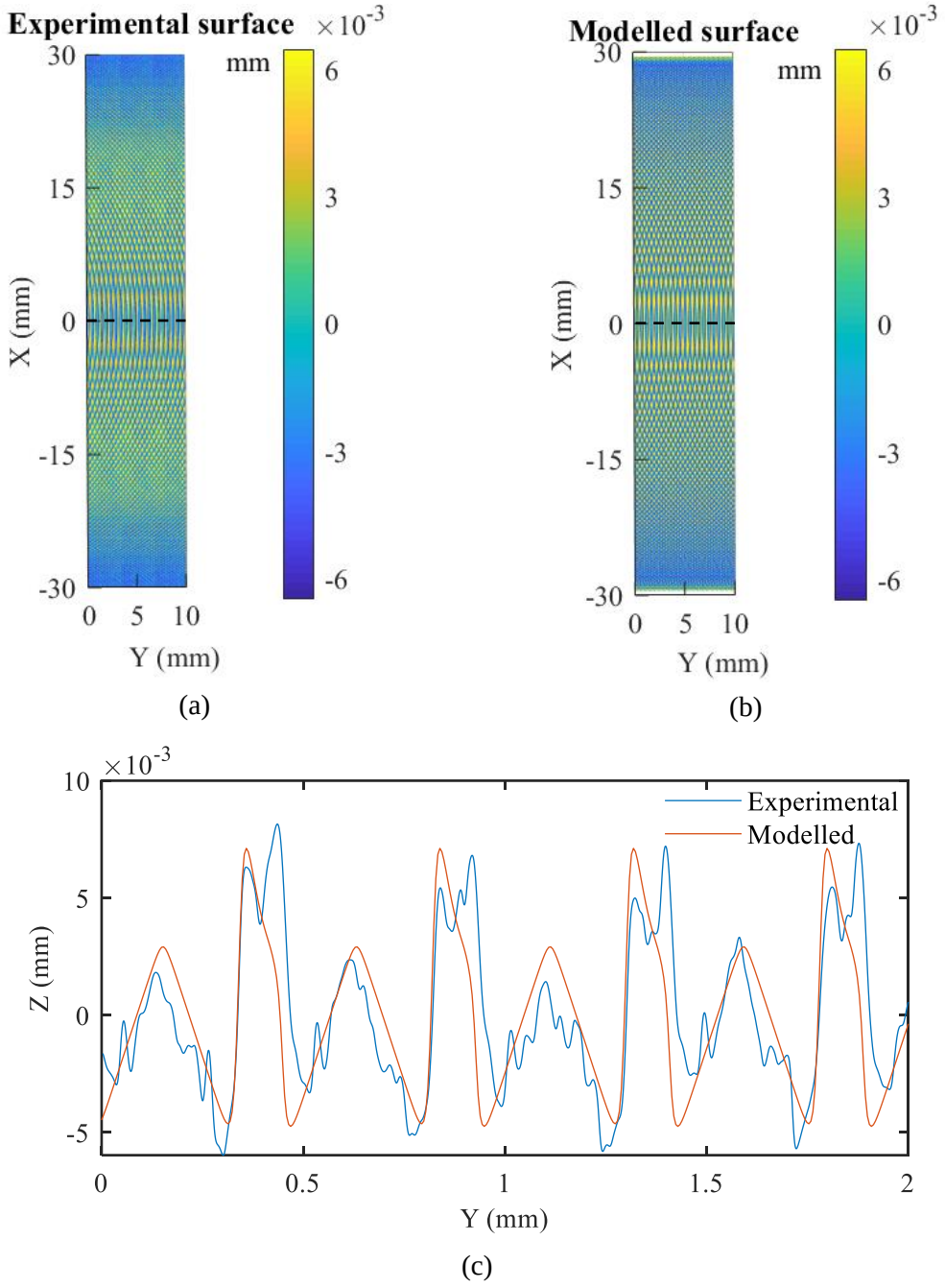

Figure 13. Comparison of experimental and modelled 2D and 3D profiles for test number 2. The black dashed line over the rough surfaces indicates the O at which the 2D roughness profile was obtained (at 0 mm), a) Experimental surface, b) Modelled surface, c) Profile comparison.

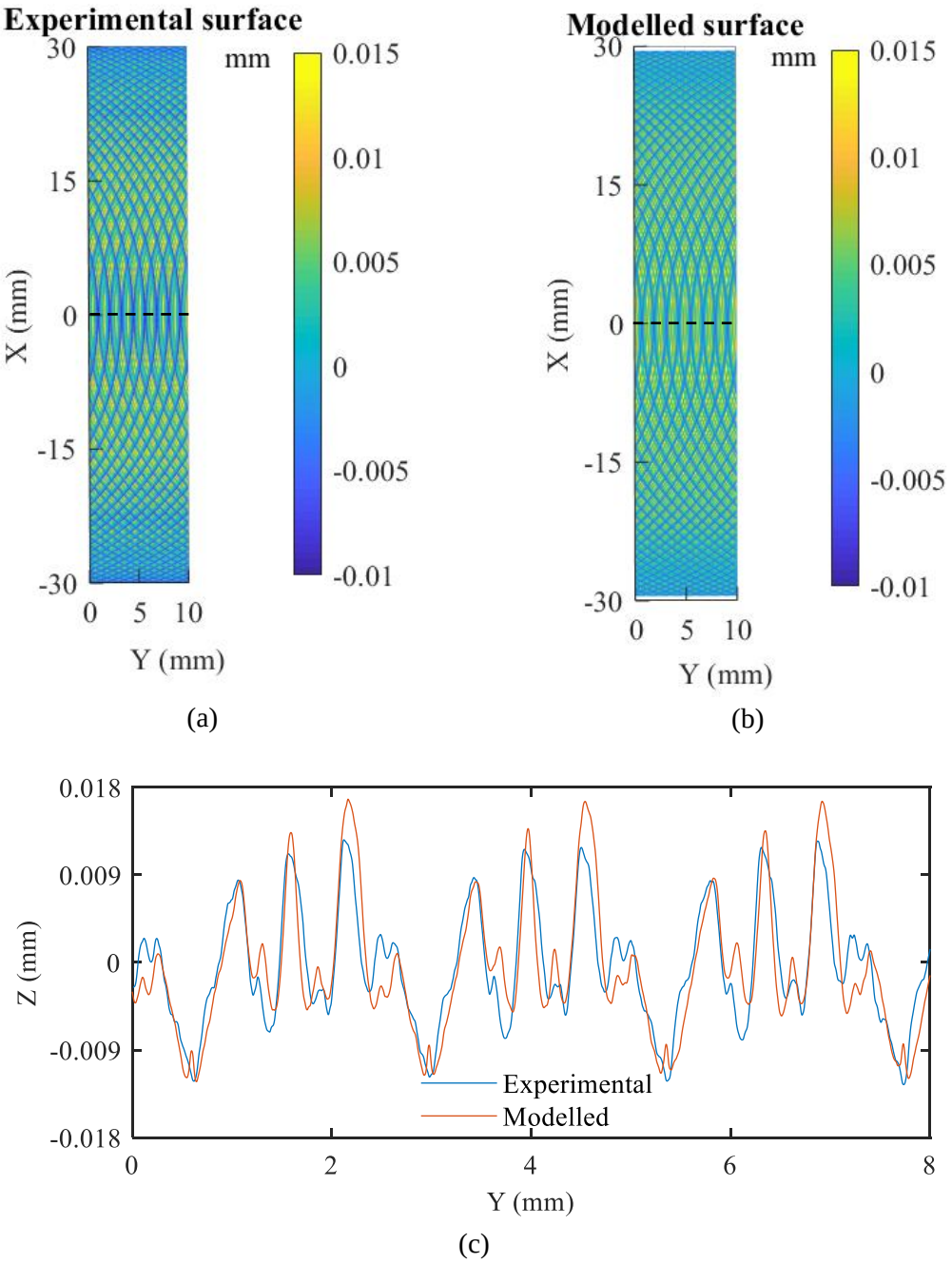

Figure 14. Comparison of experimental and modelled 2D and 3D profiles for test number 3. The black dashed line over the rough surfaces indicates the O at which the 2D roughness profile was obtained (at 0 mm), a) Experimental surface, b) Modelled surface, c) Profile comparison.

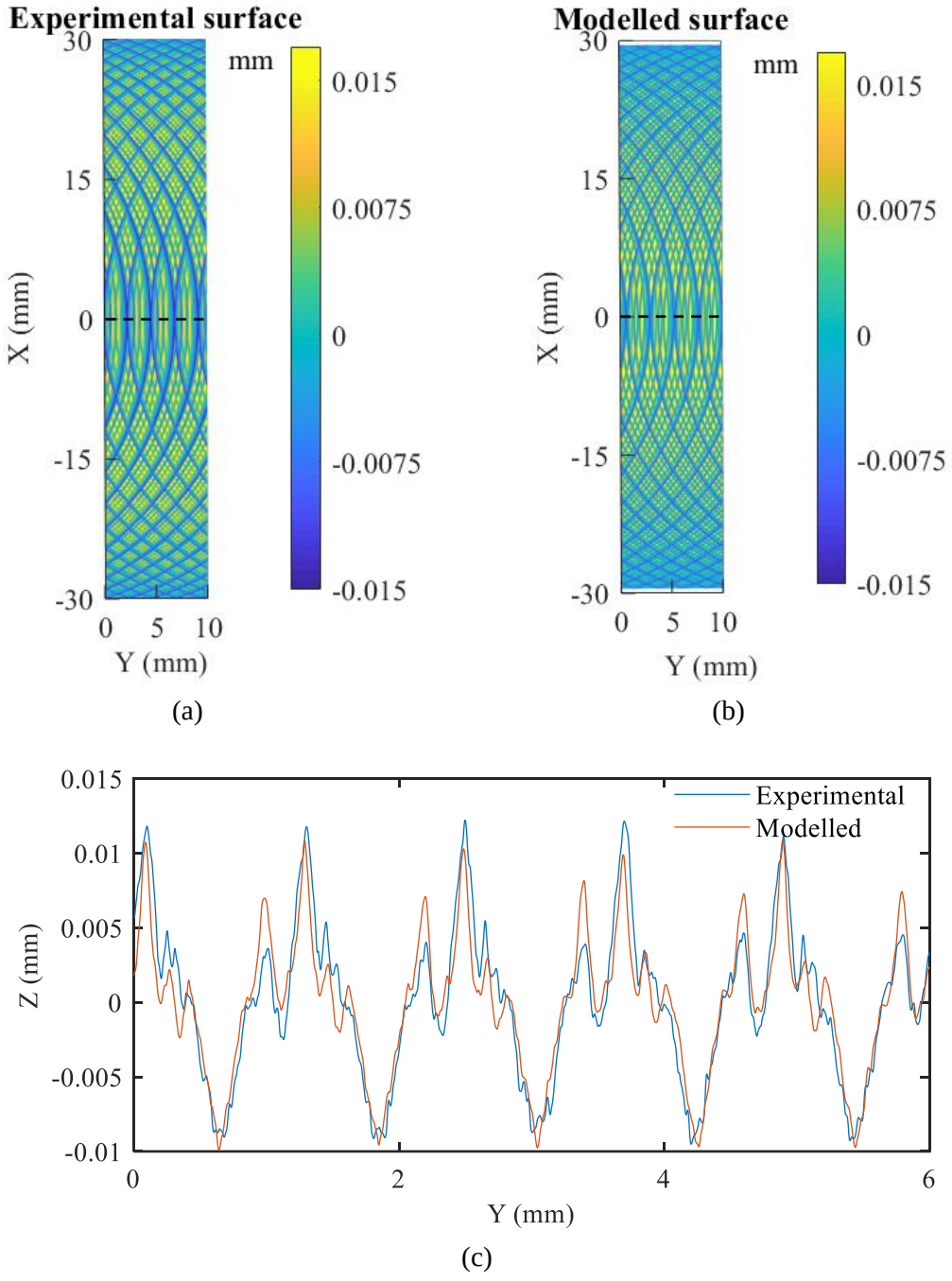

Figure 15. Comparison of experimental and modelled 2D and 3D profiles for test number 4. The black dashed line over the rough surfaces indicates the O at which the 2D roughness profile was obtained (at 0 mm), a) Experimental surface, b) Modelled surface, c) Profile comparison.

5 Sensitivity analysis of cutting conditions and geometrical parameters of the tool on the roughness surfaces

As observed in the experimental results, the cutting conditions and several tool geometry parameters significantly affect roughness in face milling, and their study is crucial for tool design and improving the performance of manufacturing processes. In this manner, the roughness predictive model developed in this research work was used to perform a sensitivity analysis. The analyses have been complemented by a series of experimental results to demonstrate their validity. The parameters studied in the analysis were (i) feed rate in section 5.1, (ii) quantity of teeth and their position in the tool (including axial and radial positions) in section 0, and (iii)

micro-geometry of the scraper and roughing teeth in section 5.3. To analyse the sensitivity of these parameters, a tool with a homogeneous tooth distribution was chosen, alternating scraper teeth with roughing teeth (1-1 distribution). The nominal geometrical parameters of the tool are shown in Table 7. R_a indicator was used to perform the analysis. These parameters vary depending on the parameter in study.

Table 7. Geometrical parameters of the scraper and roughing teeth of the mill used for the sensitivity analysis.

	Axial position (µm)	Radial position (mm)	Position in the tool	R_n (mm)	i (º)
6 scraper teeth	-15	30.5	1-3-5-7-9-11	0.5	-
6 roughing teeth	0	31.5	2-4-6-8-10-12	-	3

5.1 Influence of the feed rate (f_z)

Using the model developed in this research work, it was observed that the surface roughness increases and decreases with the feed per tooth. In addition, it was observed that these variations are non-linear with the feed per tooth, as the roughness shows a sawtooth behaviour within its upward or downward trend. Finally, it could also be observed that above a certain feed per tooth, the roughness decreases. As an example of where to observe these roughness behaviours, Figure 16 shows the results for R_a indicator for a f_z range from 0.001 mm/z to 0.4 mm/z and O 0 mm.

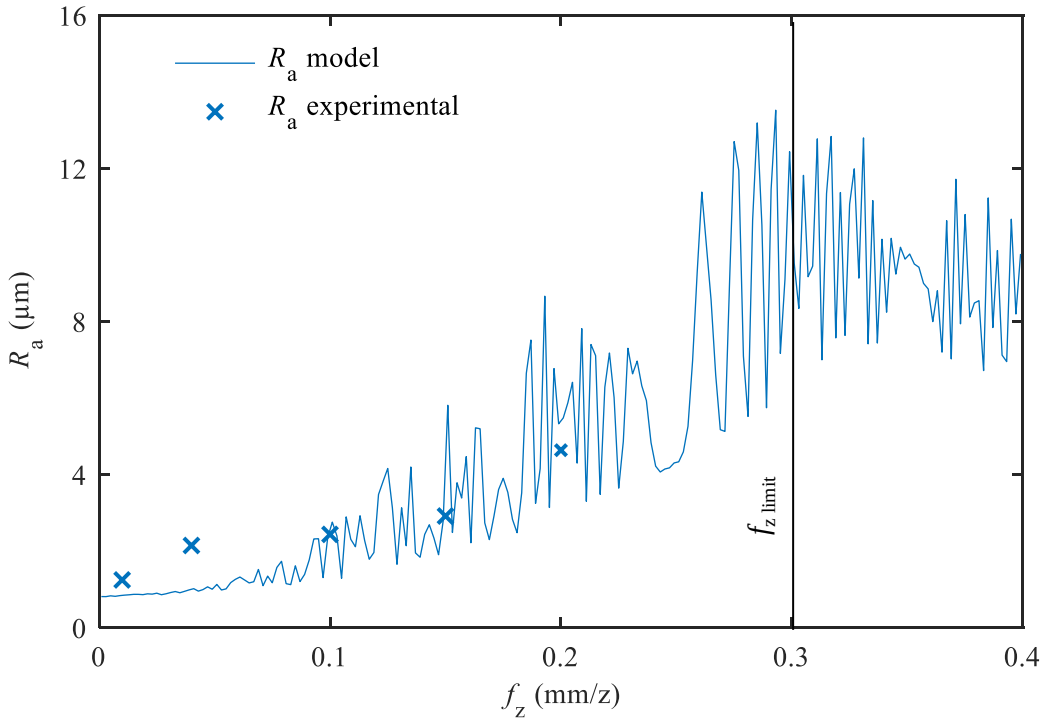

Figure 16. Modelled R_a variation with f_z at O 0 mm, and a set experimental results. R_a is observed to increase with f_z, but not linearly. In addition, above a certain f_z, the value of R_a starts to decrease ($f_{z\ limit}$). Experimental results are marked with a blue cross.

The cause of the roughness varying with the feed per tooth is that decreasing f_z, the traces left by each tooth are closer each other. Consequently, the intersections between these traces occur at a lower height, which leads to lower profile amplitudes and roughness. In contrast, increasing f_z, the traces left by each tooth are further each other, generating higher profile amplitudes and in consequence, increasing the surface roughness. This can be observed in Figure 17, where the profile amplitude is 16 µm for a f_z of 0.15 mm/z (see Figure 17 a)) and 22 µm for a f_z of 0.2 mm/z. (see Figure 17 b)). In this example, this behaviour is observed up to a f_z of approximately 0.3 mm/z.

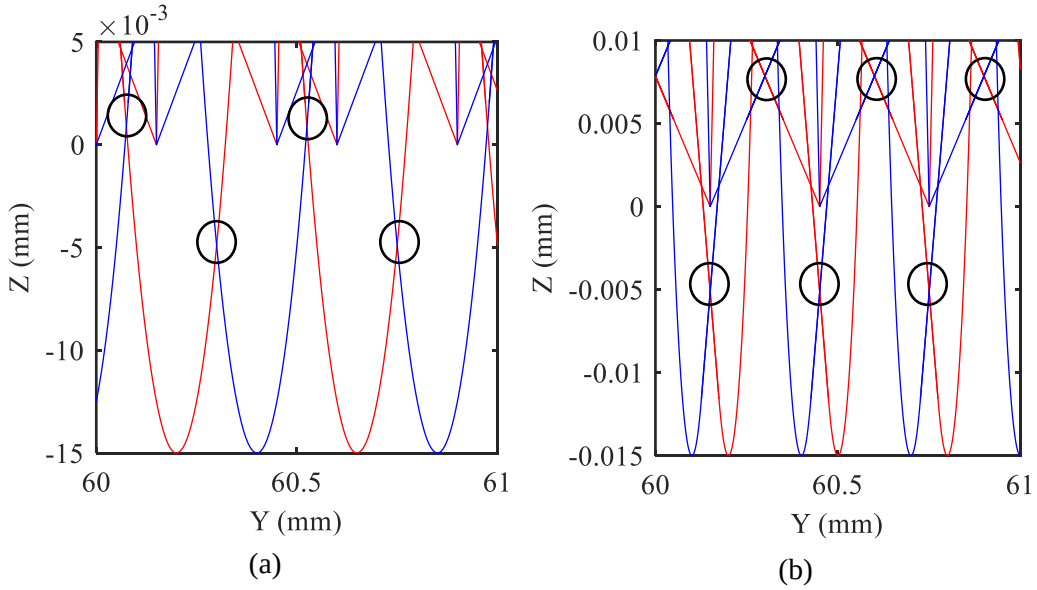

Figure 17. Influence of the feed rate over the topography of the roughness profile, a) f_z 0.15 mm/z, b) f_z 0.2 mm/z. The red lines correspond to the primary geometric profile and blue lines to the secondary roughness profile. The black circles indicate the intersection points between the traces left by each tooth, which occur at higher heights as the feed rate increases.

Moreover, it can also be observed that the roughness starts to decrease above f_z 0.3 mm/z. This phenomenon is also related to the position of the traces left by each tooth. Increasing enough the f_z, the traces generated by the scraper teeth are too far from each other that the surface is not sufficiently texturized, i.e., the density of peaks and valleys of the roughness profile is too low and it results in an excessively flat surface. In consequence, the surface roughness begins to decrease. In this manner, it is demonstrated that although Korkut and Donertas [12], Sun and Guo [15], Baek et al. [16], and Ryu et al. [52] concluded that surface roughness increases with the feed rate, the opposite effect can be achieved at high feed rates.

The feed rate at which this trend change occurs has been called as $f_{z\ limit}$. The roughness will vary with the feed per tooth to a greater or lesser extent depending on the micro-geometry of the teeth. The narrower the traces generated by the teeth (smaller radius of the scraper teeth), the greater the increase in roughness with the feed per tooth. However, $f_{z\ limit}$ will be reached at a lower feed rate.

Figure 16 also illustrates that the roughness increase is non-linear with the feed rate, as R_a values describe a sawtooth behaviour within an upward or downward trajectory. The same effect can be intuited from the experimental results (see the blue crosses in Figure 16). This phenomenon is closely related to the offset distance (O_f), defined as the offset between the primary and the secondary geometric roughness profiles. Depending on O_f, the intersections between the traces will occur differently so that within an upward or downward trajectory, there may be variations in roughness values.

5.2 Influence of the quantity and position of scraper and roughing teeth in the tool

Apart from the feed rate, the teeth quantities and their positioning in the tool influences the roughness values. In fact, roughness can vary even if the cutting conditions are not modified. This strategy could be advantageous when the cutting conditions cannot be changed due to manufacturing process requirements. To perform the analysis, several simulations were performed by modifying both the number of teeth and their position on the tool in a feed per tooth range. In Figure 18, an example is shown of the performed analysis. In this case, a f_z range between 0.001 mm/z and 0.4 mm/z, and different quantities of scraper teeth were tested: one (marked in blue), two (marked in red), four (marked in yellow), and six (marked in purple). A homogeneous distribution of teeth was chosen in each case, and roughness was measured in the centre of the tool trajectory.

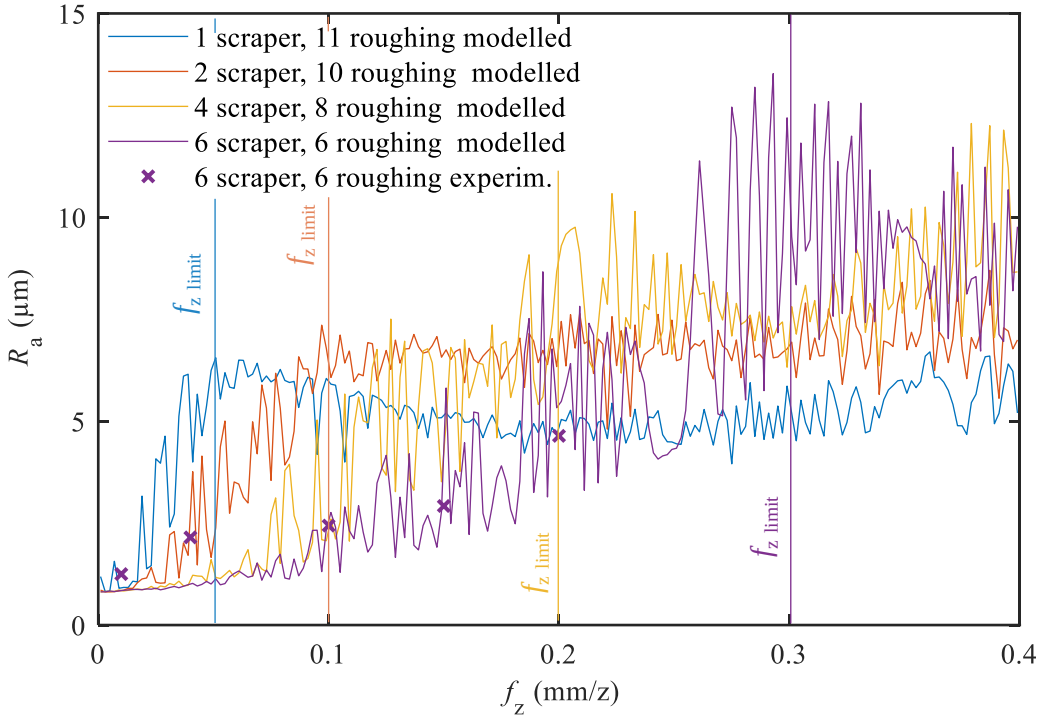

Figure 18. Modelled R_a variation with f_z at O 0 mm, considering different scraper-roughing quantity and combinations: in blue 1 T_s for 11 T_r, in orange 2 T_s for 10 T_r, in yellow 4 T_s for 8 T_r and in purple 6 T_s for 6 T_r. In all options, teeth were uniformly distributed. A set of experimental results for 6-6 teeth combination is shown with purple crosses.

As it can be observed, R_a increases with the feed rate until achieving the corresponding $f_{z\ limit}$. However, the rate of increase is different concerning the number of scraper teeth used. The lower the number of scraper teeth, the higher the growth rate at low f_z (for example, using one or two scraper teeth). In turn, the increase is more gradual with a higher number of scraper teeth. This phenomenon occurs due to the relationship between the number of traces generated on the surface and the feed rate. If the feed rate is low enough, the traces left by the scraper teeth intersect at an excessively short distance, as shown in Figure 17 a). In this case, the lower the number of scraper teeth, the higher the profile amplitude, and hence, the surface roughness. In turn, if the feed rate is high enough, the traces left by the scraper teeth intersect at an excessively long distance, as shown in Figure 17 b). In this respect, the higher the number of scraper teeth, the higher the number of traces left by the teeth, and hence, the surface roughness.

The turning point between the two trends is the denominated $f_{z\ limit}$, which is related to the feed per scraper tooth $f_{z\ scraper}$, defined as the feed rate between two traces generated by the same scraper

tooth. In fact, for the four cases studied, $f_{z\ scraper}$ was 0.6 mm/z when the roughness trend changed. $f_{z\ scraper}$ is calculated with Equation (11), which depends on $f_{z\ limit}$, teeth quantity Z and scraper teeth quantity Z_s.

$$f_{z\ scraper} = \frac{f_{z\ limit} \cdot Z}{Z_s} \tag{11}$$

One scraper tooth (marked blue in Figure 18) $f_{z\ scraper} = \frac{0.05 \cdot 12}{1} = 0.6\ mm/z_s$

Two scraper teeth (marked orange in Figure 18) $f_{z\ scraper} = \frac{0.1 \cdot 12}{2} = 0.6\ mm/z_s$

Four scraper teeth (marked yellow in Figure 18) $f_{z\ scraper} = \frac{0.2 \cdot 12}{4} = 0.6\ mm/z_s$

Six scraper teeth (marked purple in Figure 18) $f_{z\ scraper} = \frac{0.3 \cdot 12}{6} = 0.6\ mm/z_s$

In fact, Figure 19 shows that if the number of scraper teeth varies but $f_{z\ scraper}$ is maintained, roughness follows a similar behaviour in the four cases. The differences that exist are related to the effect of f_z on the O_f distance, that is, on the relative positioning between the primary and secondary geometric profiles.

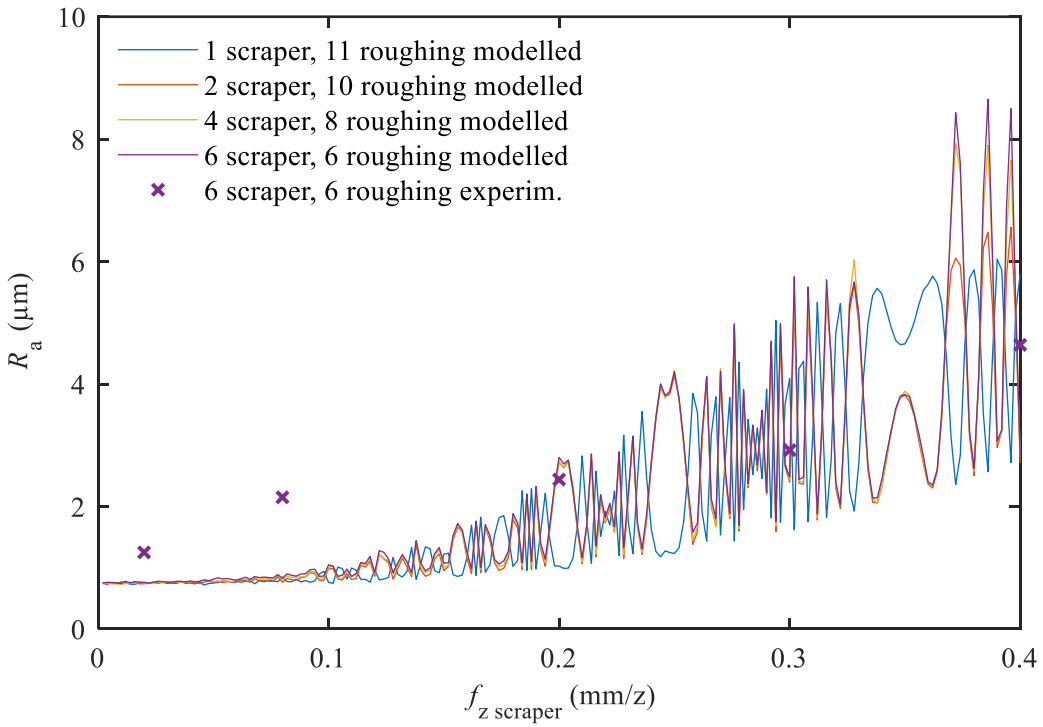

Figure 19. Evolution of R_a with regard to a different quantity and distribution of scraper teeth at O 0 mm, maintaining $f_{z\ scraper}$. In blue 1 T_s for 11 T_r, in orange 2 T_s for 10 T_r, in yellow 4 T_s for 8 T_r and in purple 6 T_s for 6 T_r. In all options, teeth were uniformly distributed. A set of experimental results for 6-6 combination is shown with purple crosses.

Analysing the trend of the roughness in the cross-feed direction of the surface, Figure 20 shows an example of the distribution of R_a for (a) a mill with one scraper tooth, and b) a mill with six scraper teeth, both for f_z 0.1 mm/z. In both cases, it can be observed how R_a has a variation of 2 µm between a maximum and a minimum value. However, when machining with a single scraper tooth, there are numerous areas where the roughness remains stable at 6 µm (see Figure 20 a)). The cause for this effect is that the number of valleys generated on the surface is few and these are homogeneously distributed across the width of cut. In consequence, a more homogeneous roughness is obtained over the complete machined surface.

In turn, having six scraper teeth, the number of traces left in the surface is higher, and the number of intersections between them increases, this being more noticeable in the outer areas of the width of cut. Consequently, the roughness values are lower (between 1-2.5 µm) and they decrease as the off-centre distance increases (see Figure 20 b)). Overall, roughness will tend to be more homogeneous with a smaller number of scraper teeth.

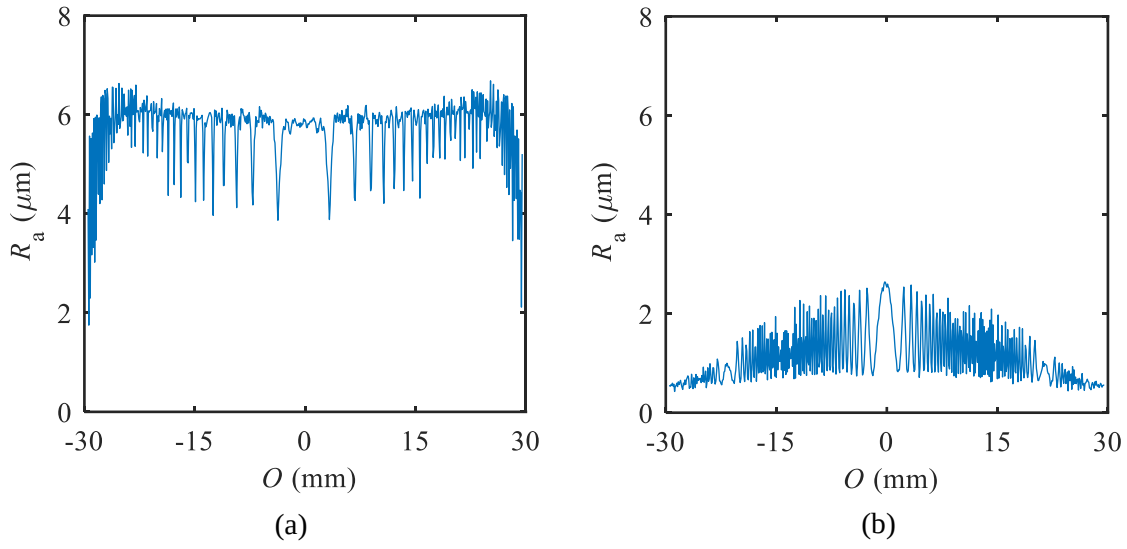

Figure 20. R_a distribution in the width of cut for f_z 0.1 mm/z, a) tool with a single scraper tooth (1 T_s-11 T_r), b) six scraper teeth (6 T_s-6 T_r). With a single scraper tooth, R_a distribution is more homogeneous, and higher values are achieved for the same cutting conditions and tool geometries.

Moreover, the position of the roughing and scraper teeth on the tool is a factor to be considered when structuring the surfaces with face milling. Within a homogeneous distribution of the inserts, there are multiple ways to allocate them in the tool, and, roughness is affected depending on how they are grouped. To analyse the influence of tooth positioning over the roughness, simulations were carried out in a feed rate range of 0.001 mm/z to 0.4 mm/z having six scraper and six roughing teeth. Teeth distribution was carried out as following: 1 scraper tooth per 1 roughing tooth (1-1) (see Figure 21 a)), 2 scraper teeth per 2 roughing teeth (2-2) (see Figure 21 b)) and 3 scraper teeth per 3 roughing teeth (3-3) (see Figure 21 c)).

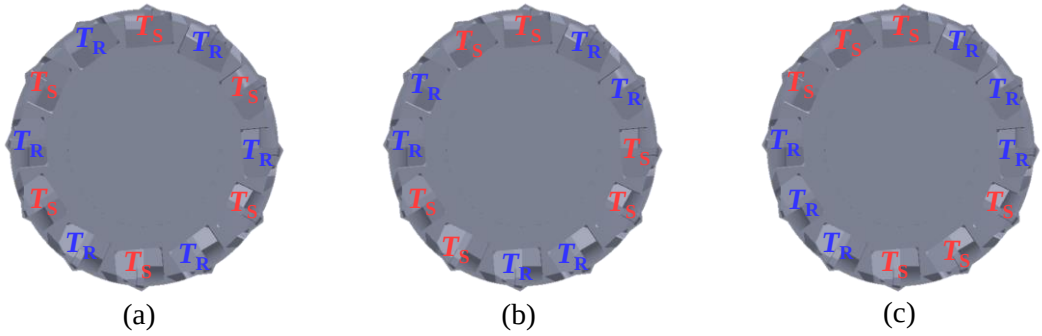

Figure 21. Different group distributions for scraper and roughing teeth (S= Scraper, R= Roughing), a) (1-1), b) (2-2), c) (3-3).

In Figure 22 a) it can be observed that the roughness is lower for the 1-1 distribution (marked in blue). These lower roughness values are related to a higher number of intersections between the traces generated over the surface. As discussed previously in this subsection, a higher number of traces leads to lower profile amplitude, which reduces the roughness values. In contrast, when the

scraper teeth are placed in groups of two or three, the traces are wider but less in number. This causes a higher profile amplitude, which increases the roughness. It can therefore be concluded that for the same number of teeth, the greater the grouping of scraper teeth, the greater the roughness achieved. This effect can also be observed in the cross-feed direction (see Figure 22 b)). For the same feed rate (f_z 0.1 mm/z in this example), the highest roughness values were obtained with the scraper teeth distributed in 3-3.

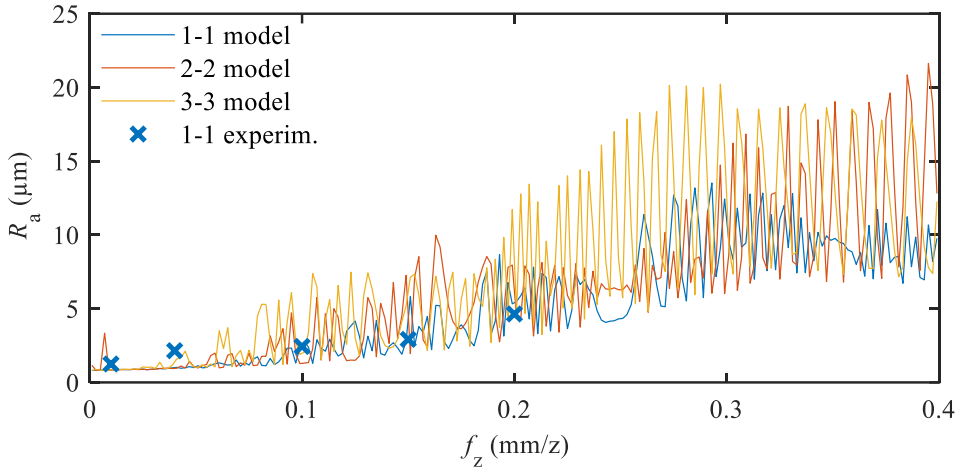

(a)

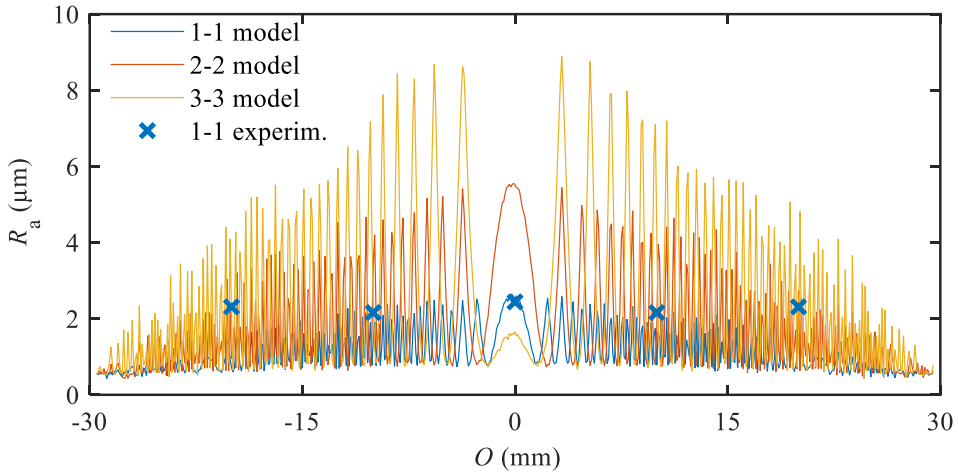

(b)

Figure 22. a) R_a variation with the feed rate for different tooth distributions at O 0 mm and b) R_a variation with the off-centre distance for different tooth distributions. For both figures, 1-1 distribution in blue, 2-2 distribution in orange, 3-3 distribution in yellow and blue crosses for experimental tests.

In addition to what has been discussed so far, the positioning of the inserts at different radii and heights has a considerable influence on the roughness. Between the two directions, the axial position of the teeth stands out, where the difference in height between the scraper and roughing inserts is defined with an axial differential distance (h_t). To analyse its influence, simulations were performed in a range of f_z between 0.001 mm/z and 0.4 mm/z at O 0 mm, positioning the scraper teeth 15 µm and 20 µm lower than the roughing teeth.

As observed in Figure 23, if the feed rate is low enough, h_t does no influence the roughness values. The reason is that the feed rate is so low that the traces generated by the scraper teeth only intersect between them (see Figure 24 a)). Therefore, as the roughing teeth do not participate generating

the roughness profiles, the h_t parameter is not relevant at this f_z range (until 0.21 mm/z for this tool geometry). The f_z range where the roughing teeth do not affect the roughness will vary depending on the insert geometries, as the smaller the nose radius of the scraper teeth, the lower this f_z range, and as the bigger the nose radius, the higher this f_z range.

However, if the feed rate is increased sufficiently (above f_z 0.21 mm/z for this tool geometry), the traces generated by the scraper teeth become so far apart that the roughing teeth machine the peaks appearing between them. In such cases, the axial differential distance influences the roughness since the greater the axial differential distance, the higher the roughness obtained.

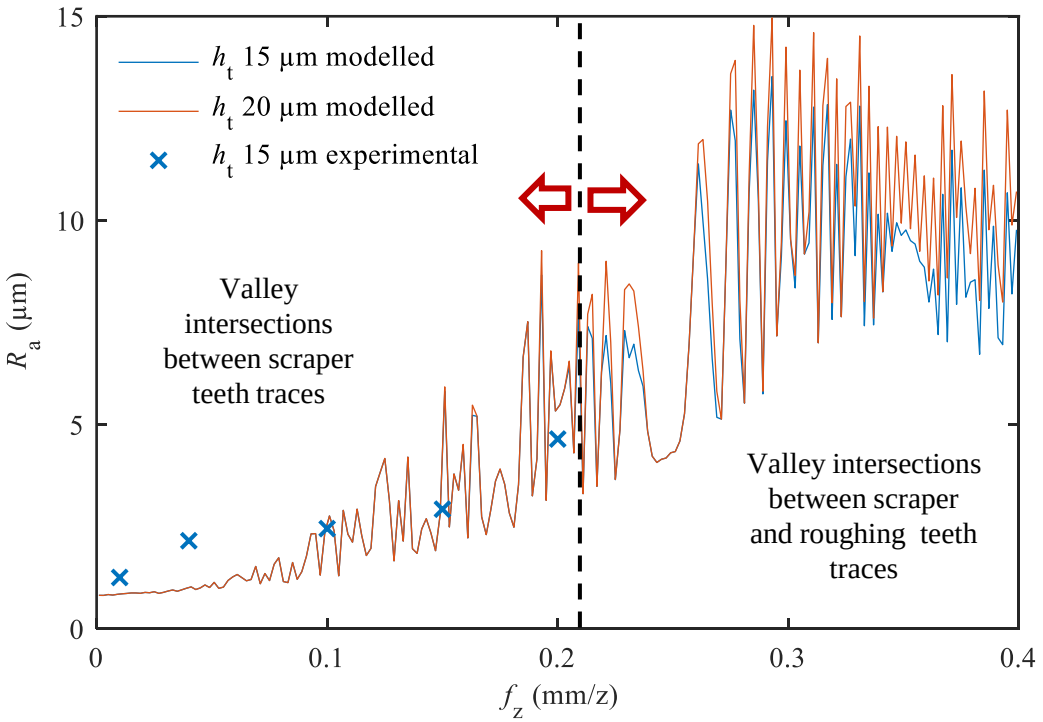

Figure 23. R_a variation with f_z at O 0 mm having scraper teeth at -15 µm (blue) and -20 µm (orange) below the roughing teeth. Experimental results for h_t 15 µm are shown with blue crosses. It can be observed that below a critical f_z, no differences are observed. Nevertheless, above a critical f_z, a higher h_t means a higher roughness.

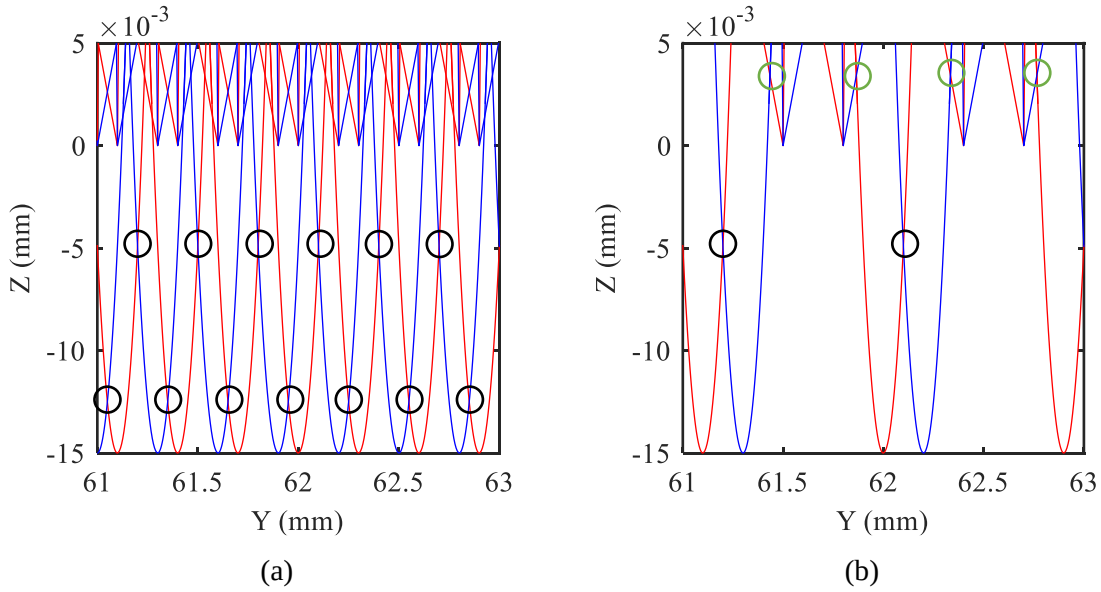

Figure 24. a) Intersection points between primary and secondary geometric roughness profiles at a) 0.1 mm/z and b) 0.3 mm/z. The intersections indicated in black colour occur only between the traces of the scraper teeth. The intersections indicated in green occur between the traces of the scraper and roughing teeth.

Moreover, it is possible to modify the roughness of the complete range of f_z by increasing the axial differential distance of a part of the scraper teeth. In the example shown in Figure 25, scraper teeth 1 and 4 were lowered to -20 µm ~~(marked with a white S in the diagram on the left side of the figure)~~, maintaining scraper teeth 7 and 10 at -15 µm. As it can be observed, roughness increases for the complete range of feed rates. Although at the lower feed rates intersections only occur between the traces generated by the scraper teeth, the axial differences of 5 µm between them generate higher profile amplitudes regardless of the feed rate.

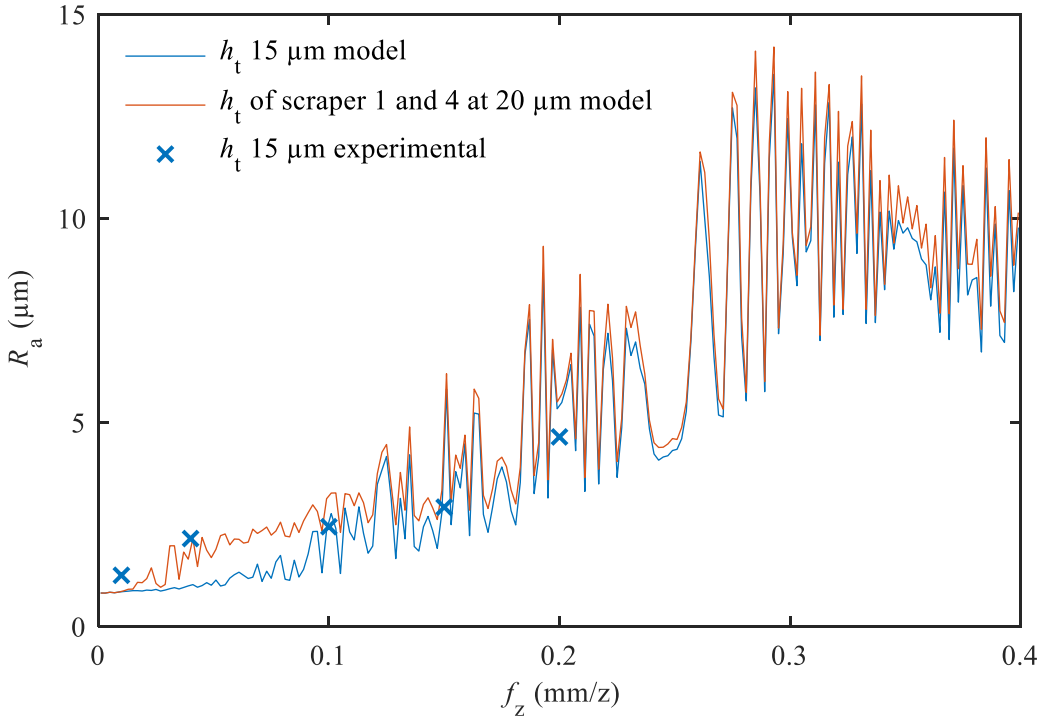

Figure 25. R_a variation with f_z at O 0 mm having all scraper teeth at -15 µm (blue in the graph), only scraper teeth 1 and 4 at -20 µm (orange in the graph and white S in the scheme of the right) and experimental (blue crosses). It can be

seen how increasing the h_t of two of the scraper teeth increases the roughness in the complete f_z range. S = Scraper, R = Roughing.

Finally, the effect of varying the radial differential distance (r_t) between the scraper and roughing teeth was analysed. For this purpose, simulations were carried out varying the radial positions of the scraper teeth while fixing the position of the roughing teeth. In the example shown in Figure 26, the scraper teeth were placed at diameters of 61 mm, 62 mm and 63 mm, while the roughing teeth were maintained at a diameter of 63 mm. In that way, the radial differential distance between scraper and roughing teeth was varied 2 mm, 1 mm and 0 mm. It can be observed how changing r_t does not increase or decrease the roughness values. Changing this parameter leads to a different roughness distribution across the machined surface, but does not change the magnitude of the roughness values.

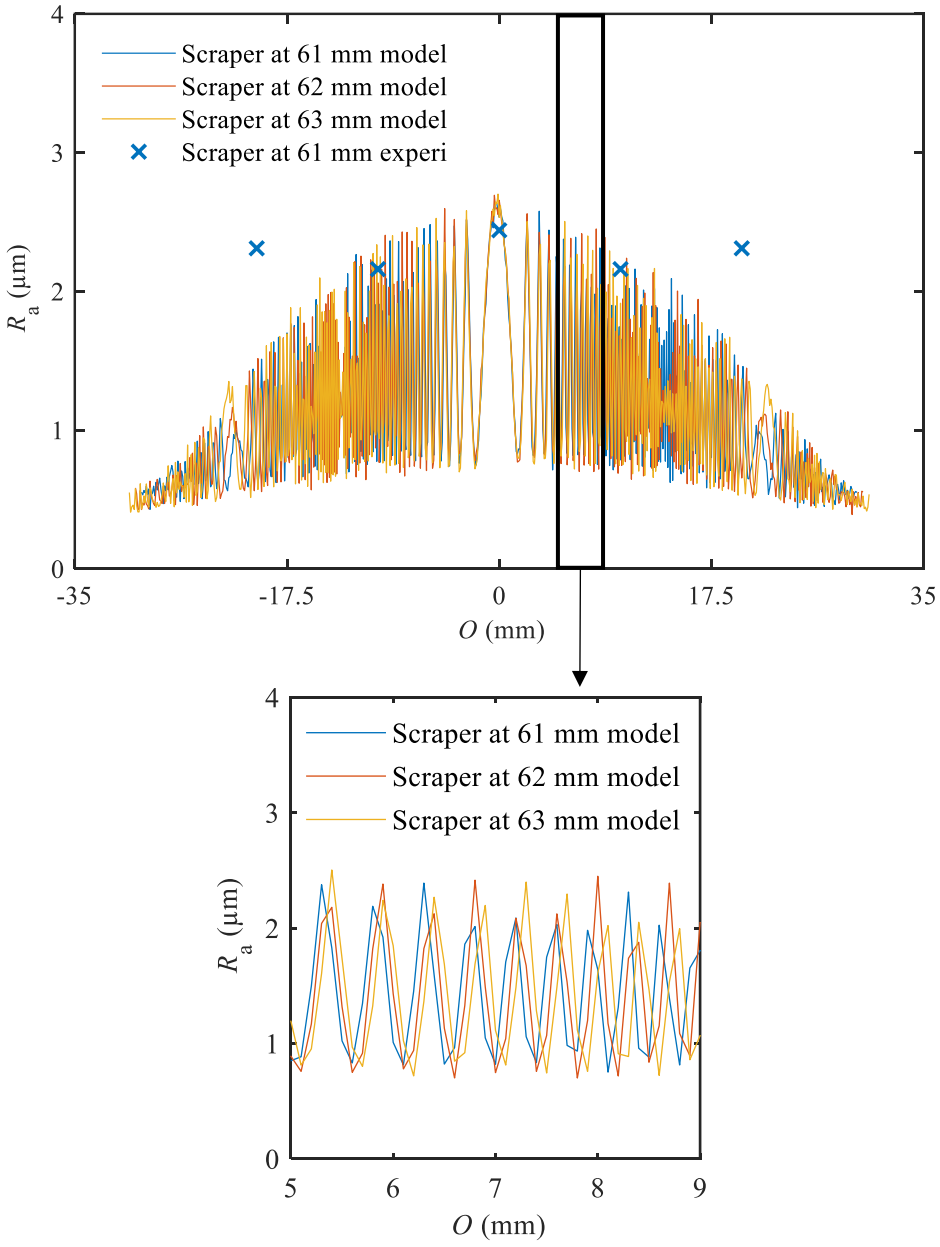

Figure 26. R_a variation in the width of cut with scraper teeth at different diameters: at 61 mm (blue), at 62 mm (orange), 63 mm (yellow) and experimental at 61 mm (blue crosses). It can be observed how the magnitude of the roughness indicators do not change, but occurs a redistribution of the roughness in the width of cut.

The diameter of the tool is a critical parameter that affects the offset between the primary and secondary geometric roughness profiles, as shown in Equation (4). Nevertheless, it does not affect the amplitude of the roughness profile or to the number of traces left in the surface. In fact, the peaks and valleys are displaced to other off-centre distances, redistributing the roughness values.

5.3 Influence of the micro-geometry of scraper and roughing teeth

To finish with the analysis, the effect of varying parameters related to the micro-geometry of the inserts was analysed. In this manner, it can be possible to modify the roughness values even if the feed rate and the number and position of the inserts in the tool are fixed. In this subsection, the effects of the nose radius of the scraper teeth (R_n) and the end-edge angle of roughing teeth (i) are analysed.

In order to analyse the influence of R_n, its nominal value of 0.5 mm was increased to 1 mm and decreased to 0.1 mm and 0.01 mm. Figure 27 shows that for a determined f_z (0.1 mm/z in this example) R_a can be considerably modified in the cross-feed direction with the nose radius of the scraper teeth.

If R_n is such that the amplitude of the roughness profile is high (low R_n at low f_z and high R_n at high f_z,), high roughness values are achieved (see Figure 27 for R_n 0.01 mm and 0.1 mm). Nevertheless, if R_n is large enough that the roughness profile amplitude is low (high R_n at low f_z and low R_n at high f_z), roughness indicators are considerably reduced (see Figure 27 for R_n 0.5 mm and 1 mm).

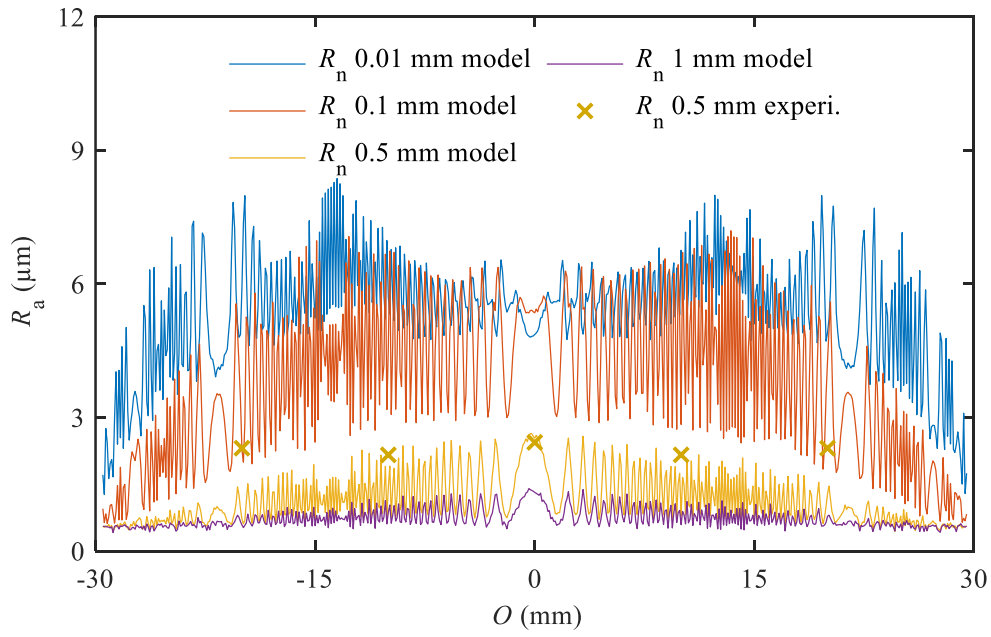

Figure 27. R_a variation with different R_n across the width of cut, for f_z 0.1 mm/z: R_n 0.01 mm (blue), R_n 0.1 mm (orange), R_n 0.5 mm (yellow) and R_n 1 mm (purple) and experimental R_n 0.5 mm (yellow crosses). It can be observed how the highest roughness is achieved with the smallest R_n. and the lowest roughness with the highest R_n.

Performing the analysis in the centre of the tool trajectory and in a wide range of R_n values (see Figure 28), it can be observed how increasing R_n the roughness increases up to a limit value (R_n 0.11 mm). From this limit value, the traces generated by the scraper teeth become wider, which decreases the amplitude of the roughness profile, and R_a starts to decrease (see Figure 28 for R_n 1 mm). Finally, R_a tends to stabilise, so that increasing R_n has no major impact on roughness.

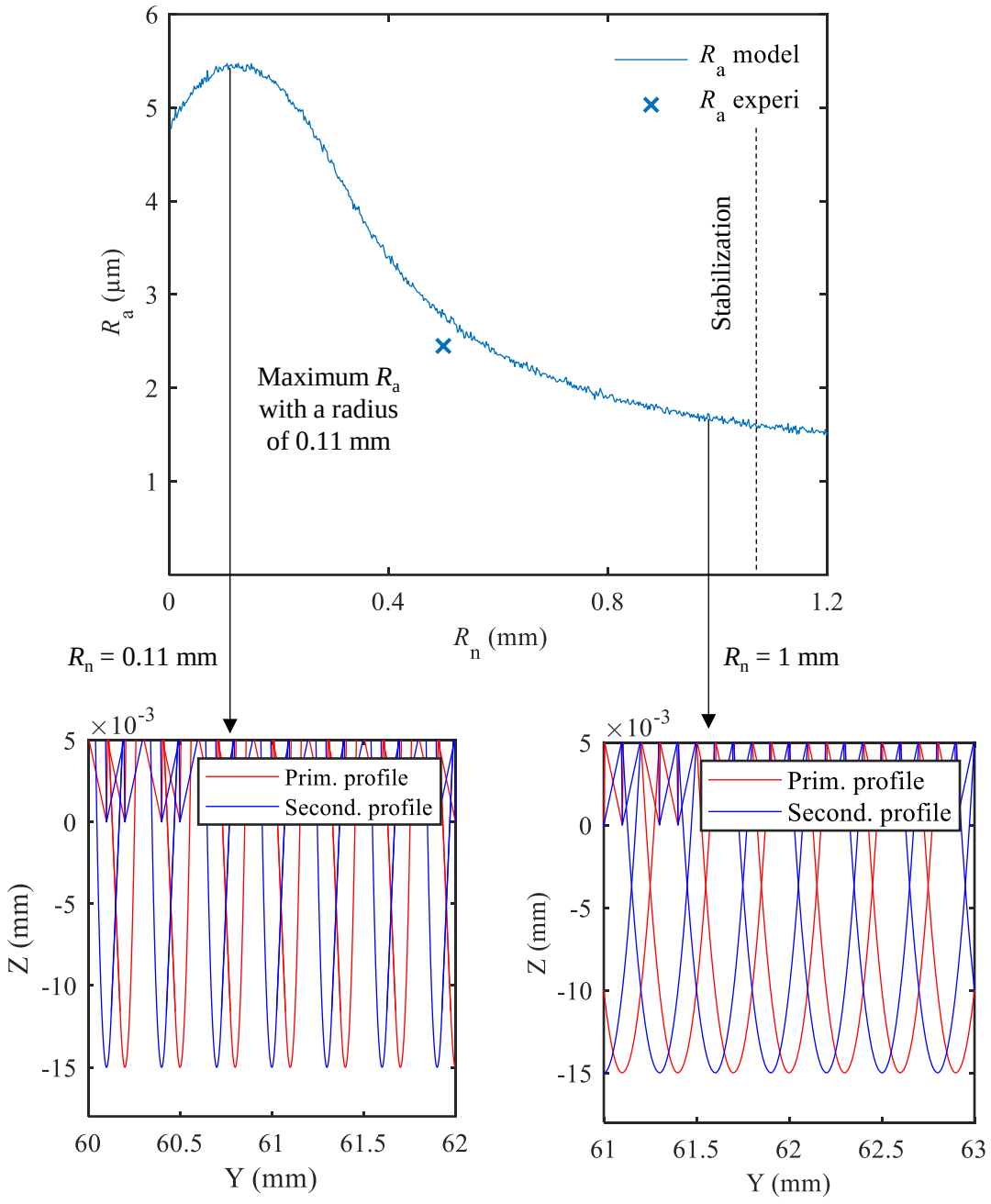

Figure 28. R_a evolution with different R_n at O 0 mm for f_z 0.1 mm/z. An experimental result is shown with a blue cross. The maximum roughness is achieved with a R_n of 0.11 mm, above that value, roughness decreases.

Moreover, Figure 29 shows how varying f_z the surface roughness is different depending on the R_n values. In the lower feed rates, the intersections between the traces left by the scraper teeth occur at shorter distances, resulting in low profile amplitudes and roughness values. And if, in addition, the nose radius value increases, the roughness value decreases even more, as shown in Figure 29 until f_z 0.23 mm/z. If it is intended to increase the roughness values in that range of feed rates, it is necessary to decrease the value of the nose radius in order to increase the amplitude of the roughness profile, and consequently the surface roughness. In contrast, when the feed rate increases, the traces generated by the teeth are more separated between them, and the higher roughness values are achieved by the highest nose radii.

From this analysis can be concluded that depending on the feed rate to be worked at, the nose radius of the scraper teeth is a crucial parameter to obtain the desired roughness value.

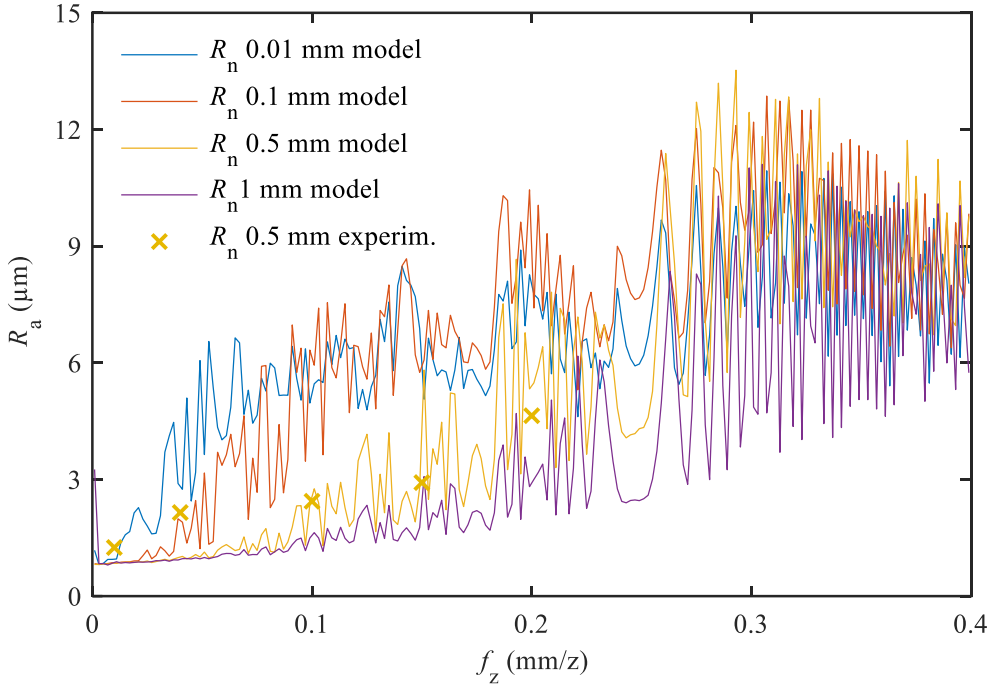

Figure 29. R_a variation with f_z at O 0 mm for R_n 0.01 mm (blue), R_n 0.1 mm (orange), R_n 0.5 mm (yellow), R_n 1 mm (purple) and experimental for R_n 0.5 mm (yellow crosses). It is observed how roughness increases with the feed rate, but at different growth rates depending on R_n.

Finally, in order to analyse the effect of the end-edge angle of the roughing teeth (*i*), simulations were carried out at 3º, 6º and 9º, maintaining the rest of the geometrical parameters as constant. Figure 30 shows that below a given feed rate (0.21 mm/z in this example), the end-edge angle does not influence the roughness values. The reason is that the feed rate is low enough so that the traces generated by the scraper teeth only intersect each other, as shown in Figure 24 a), and the roughing teeth do not intervene in the roughness profile generation.

However, at higher feed rates (above 0.21 mm/z in this example), the traces left by the scraper teeth are sufficiently separated to allow the roughing teeth to machine the peaks that appear between them, as shown in Figure 24 b). In these cases, the greater the end-edge angle, the greater the peaks left over the surface, increasing the roughness values.

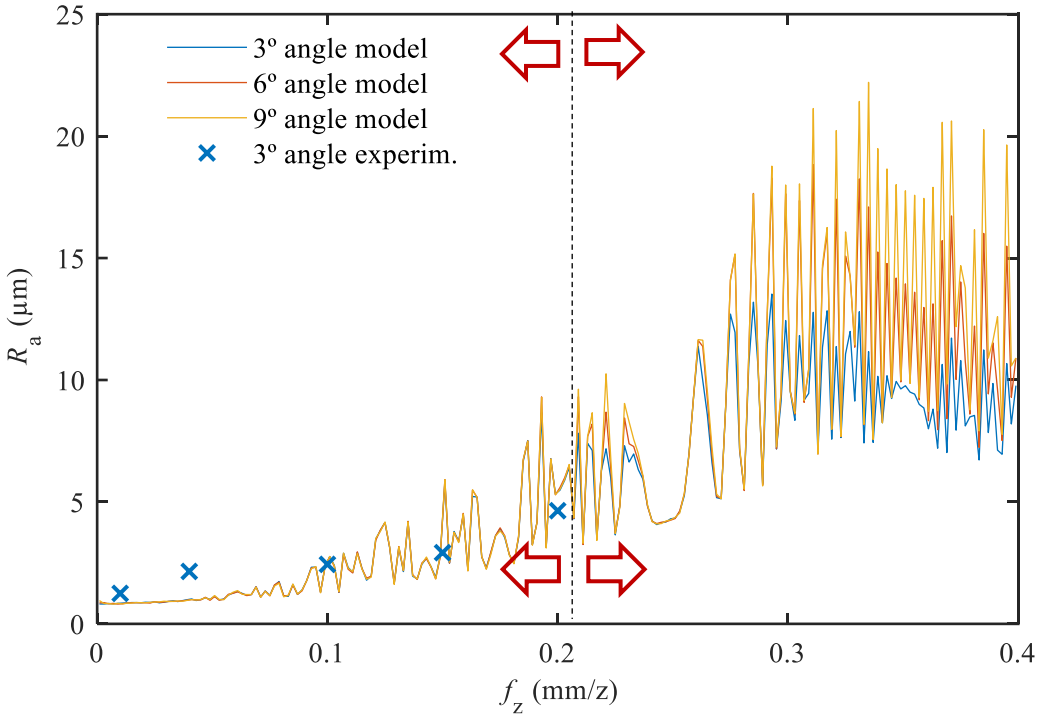

Figure 30. R_a variation with f_z at O 0 mm for i = 3º (blue), i = 6º (orange), i = 9º (yellow) and experimental i = 3º (blue crosses). No differences are observed if the intersections only occur between scraper teeth traces. If intersections occur between scraper and roughing teeth traces, roughness increases by increasing i angle.

6 Conclusions

In this work, novel roughness maps are presented as an efficient optimisation procedure to considerably reduce trial-and-error strategies. The maps provide the optimum cutting conditions and tool geometry faster than performing individual simulations or experimental tests. Moreover, the maps permit identifying the maximum possible feed rate to increase the productivity of the process and the maximum nose radius to minimise the effect of tool wear, all in compliance with the roughness requirements.

In order to calculate the roughness maps, a predictive model for surface roughness was developed based on 3D face milled surfaces. The 3D surfaces were modelled as a split signal in two components: (i) the kinematic movements of the cutting edge and its geometry, and (ii) a novel approach considering the stochastic roughness, which embraces the chip removal process, material defects or vibrations. Considering the stochastic roughness, predictions improved between 27%-76% for R_{max}, $R_{z,}$ and R_t, and in a lesser extent for R_a.

In addition, a sensitivity analysis was carried out about the feed rate and several geometrical parameters of the tool. During this analysis, it was concluded that apart from the feed rate, the number of scraper and roughing teeth, the axial position of the teeth in the tool and the microgeometry of the teeth (nose radius of the scraper teeth and end-edge angle of the roughing teeth) are also important parameters to consider when structuring the surface roughness by face milling.

Acknowledgements

Authors would like to thank to the Basque government for the financial support received for the project OptiPCD (ZL-2020/00305) and FRONTIERS V (KK-2019/00077).

References

[1] I. Milne, R. O. Ritchie and B. L. & Karihaloo, Comprehensive Structural Integrity, vol. 8, Elsevier, 2003.

[2] D. G. Coblas, A. Fatu, A. Maoui and M. Hajjam, "Manufacturing textured surfaces: State of art and recent developments," *Proceedings of the institution of mechanical engineers,* vol. 1, no. 229, pp. 3-29, 2015.

[3] M. Kok, D. Raps and T. M. Young, "Effects of surface roughness and energy on insect residue adhesion to aircraft leading edge surfaces," *Proceeding of the 36th annual meeting of the adhesion society,* pp. 3-6, 2013.

[4] B. N. Persson, O. Albohr, U. Tartaglino, A. I. Volokitin and E. Tosatti, "On the nature of surface roughness with application to contact mechanics, sealing, rubber friction and adhesion," *Journal of physics: Condensed matter,* vol. 1, no. 17, 2004.

[5] M. V. dos Santos, C. N. Elias and J. H. Cavalcanti Lima, "The effects of superficial roughness and design on the primary stability of dental implants," *Clinical implant dentistry and related research,* vol. 13, no. 3, pp. 215-223, 2011.

[6] C. N. Elias, Y. Oshida, J. H. C. Lima and C. A. Muller, "Relationship between surface properties (roughness, wettability and morphology) of titanium and dental implant removal torque," *Journal of the mechanical behavior of biomedical materials,* vol. 1, no. 3, pp. 234-242, 2008.

[7] C. F. Caravaca, "Modified functional surfaces for increased biointegration: Surface chemistry, mechanical integrity and long-term stability of zirconia and alumina based ceramics," 2016.

[8] K. Mumtaz and N. Hopkinson, "Top surface and side roughness of Inconel 625 parts processed using selective laser melting," *Rapid Prototyping Journal,* 2009.

[9] R. L. Hecker and S. Y. Liang, "Predictive modeling of surface roughness in grinding," *International Journal of Machine Tools and Manufacture,* vol. 8, no. 43, pp. 755-761, 2003.

[10] I. Buj-Corral and J. Vivancos-Calvet, "Roughness variability in the honing process of steel cylinders with CBN metal bonded tools," *Precision Engineering,* vol. 2, no. 35, pp. 289-293, 2011.

[11] P. G. Benardos and G. C. Vosniakos, "Predicting surface roughness in machining: a review," *International journal of machine tools and manufacture,* vol. 43, no. 8, pp. 833-844, 2003.

[12] I. Korkut and M. A. Donertas, "The influence of feed rate and cutting speed on the cutting forces, surface roughness and tool – chip contact length during face milling," *Materials & design,* vol. 28, no. 1, pp. 308-312, 2007.

[13] M. Alauddin, M. A. El Baradie and M. S. J. Hashmi, "Computer-aided analysis of a surface-roughness model for end milling," *Journal of Materials Processing Technology,* vol. 55, no. 2, pp. 123-127, 1995.

[14] N. S. K. Reddy and P. V. Rao, “Experimental investigation to study the effect of solid lubricants on cutting forces and surface quality in end milling,” *International Journal of Machine Tools and Manufacture,* vol. 46, no. 2, pp. 189-198, 2006.

[15] J. Sun and Y. B. Guo, “A comprehensive experimental study on surface integrity by end milling Ti-6Al-4V,” *Journal of Materials Processing Technology,* vol. 209, no. 8, pp. 4036-4042, 2009.

[16] D. K. Baek, T. J. Ko and H. S. Kim, “Optimization of feedrate in a face milling operation using a surface roughness model,” *International Journal of Machine Tools and Manufacture,* vol. 41, no. 3, pp. 451-462, 2001.

[17] L. N. Lopez de la Calle, J. Perez, J. I. Llorente and J. A. Sanchez, “Advanced cutting conditions for the milling of aeronautical alloys,” *Journal of Materials Processing Technology,* vol. 100, pp. 1-11, 2000.

[18] X. Lu, X. Wang, J. Sun, H. Zhang and Y. Feng, “The influence factors and prediction of curve surface roughness in micro-milling nickel-based superalloy,” *International Manufacturing Science and Engineering Conference,* pp. 1-6, 2018.

[19] A. Arizmendi and A. Jimenez, “Modelling and analysis of surface topography generated in face milling operations,” *International Journal of Mechanical Sciences,* vol. 163, p. 105061, 2019.

[20] M. Y. Wang and H. Y. Chang, “Experimental study of surface roughness in slot end milling AL2014-T6,” *International Journal of Machine Tools and Manufacture,* vol. 44, no. 1, pp. 51-57, 2004.

[21] R. Baptista and J. A. Simoes, “Three and five axes milling of sculptured surfaces,” *Journal of materials processing technology,* vol. 103, no. 3, pp. 398-403, 2000.

[22] E. O. Ezugwu, J. Bonney, R. B. Da Silva and O. Cakir, “Surface integrity of finished turned Ti–6Al–4V alloy with PCD tools using conventional and high pressure coolant supplies,” *International Journal of Machine Tools and Manufacture,* vol. 47, no. 6, pp. 884-891, 2007.

[23] Y. H. Tsai, J. C. Chen and S. J. Lou, “An in-process surface recognition system based on neural networks in end milling cutting operations,” *International Journal of Machine Tools and Manufacture,* vol. 39, no. 4, pp. 583-605, 1999.

[24] P. G. Benardos and G. C. Vosniakos, “Prediction of surface roughness in CNC face milling using neural networks and Taguchi's design of experiments,” *Robotics and Computer-Integrated Manufacturing,* vol. 18, no. 5, pp. 343-354, 2002.

[25] M. I. Hossain, A. N. Amin and A. U. Patwari, “Development of an artificial neural network algorithm for predicting the surface roughness in end milling of Inconel 718 alloy,” *2008 International Conference on Computer and Communication Engineering,* pp. 1321-1324, 2008.

[26] Z. Liu, D. Zhang and H. Qi, “Surface roughness modeling of high speed machining TC4 based on artificial neural network method,” *2006 1st International Symposium on Systems and Control in Aerospace and Astronautics,* pp. 920-924, 2006.

[27] T. Y. Wu and K. W. Lei, "Prediction of surface roughness in milling process using vibration signal analysis and artificial neural network," *The International Journal of Advanced Manufacturing Technology,* vol. 102, no. 1, pp. 305-314, 2019.

[28] S. Palani and U. Natarajan, "Prediction of surface roughness in CNC end milling by machine vision system using artificial neural network based on 2D Fourier transform," *The International Journal of Advanced Manufacturing Technology,* vol. 54, no. 9, pp. 1033-1042, 2011.

[29] G. Kant and K. S. Sangwan, "Predictive modelling and optimization of machining parameters to minimize surface roughness using artificial neural network coupled with genetic algorithm," *Procedia CIRP,* vol. 31, pp. 453-458, 2015.

[30] G. Mahesh, S. Muthu and S. R. Devadasan, "Prediction of surface roughness of end milling operation using genetic algorithm," *The International Journal of Advanced Manufacturing Technology,* vol. 77, no. 1, pp. 369-381, 2015.

[31] A. Yeganefar, S. A. Niknam and R. Asadi, "The use of support vector machine, neural network, and regression analysis to predict and optimize surface roughness and cutting forces in milling," *The International Journal of Advanced Manufacturing Technology,* vol. 105, no. 1, pp. 951-965, 2019.

[32] K. Kadirgama, M. M. Noor and M. M. Rahman, "Optimization of surface roughness in end milling using potential support vector machine," *Arabian Journal for Science and Engineering,* vol. 37, no. 8, pp. 2269-2275, 2012.

[33] B. O. H. &. K. H. Ozcelik, "Optimum surface roughness in end milling Inconel 718 by coupling neural network model and genetic algorithm," *The International Journal of Advanced Manufacturing Technology,* vol. 27, no. 3, pp. 234-241, 2005.

[34] H. Oktem, T. Erzurumlu and F. Erzincanli, "Prediction of minimum surface roughness in end milling mold parts using neural network and genetic algorithm," *MAterials & Design,* vol. 27, no. 9, pp. 735-744, 2006.

[35] B. P. Huang, J. C. Chen and Y. Li, "Artificial-neural-networks-based surface roughness Pokayoke system for end-milling operations," *Neurocomputing,* vol. 71, no. 4, pp. 544-549, 2008.

[36] H. Oktem, "An integrated study of surface roughness for modelling and optimization of cutting parameters during end milling operation," *The International Journal of Advanced Manufacturing Technology,* vol. 43, no. 9, pp. 852-861, 2009.

[37] I. Escamilla, P. Perez, L. Torres, P. Zambrano and B. Gonzalez, "Optimization using neural network modeling and swarm intelligence in the machining of titanium (Ti 6Al 4V) alloy," *2009 Eighth Mexican International Conference on Artificial Intelligence,* pp. 33-38, 2009.

[38] R. L. Malghan, K. M. Rao, A. K. Shettigar, S. S. Rao and R. J. D'Souza, "Application of particle swarm optimization and response surface methodology for machining parameters optimization of aluminium matrix composites in milling operation," *Journal of the Brazilian Society of Mechanical Sciences,* vol. 39, no. 9, pp. 354-3553, 2017.

[39] A. M. Pinar, S. Filiz and B. S. Unlu, “A comparison of cooling methods in the pocket milling of AA5083-H36 alloy via Taguchi method,” *The International Journal of Advanced Manufacturing Technology*, vol. 83, no. 9, pp. 1431-1440, 2016.

[40] A. M. Zain, H. Haron and S. Sharif, “Prediction of surface roughness in the end milling machining using Artificial Neural Network,” *Expert Systems with Applications,* vol. 37, no. 2, pp. 1755-1768, 2010.

[41] V. A. Tipnis, S. C. Buescher and R. C. Garrison, “Mathematically modeled machining data for adaptive control of end milling operations,” *Proc. NAMRC-iv,* pp. 279-286, 1976.

[42] M. Alauddin, M. A. El Baradie and M. S. J. Hashmi, “Optimization of surface finish in end milling Inconel 718,” *Journal of Materials Processing Technology,* vol. 56, no. 1, pp. 54-65, 1996.

[43] A. Mansour and H. Abdalla, “Surface roughness model for end milling: a semi-free cutting carbon casehardening steel (EN32) in dry condition,” *Journal of Materials Processing Technology,* vol. 124, no. 1, pp. 183-191, 2002.

[44] N. Liu, S. B. Wang, Y. F. Zhang and W. F. Lu, “A novel approach to predicting surface roughness based on specific cutting energy consumption when slot milling Al-7075,” *International Journal of Mechanical Sciences,* vol. 118, pp. 13-20, 2016.

[45] P. Muñoz-Escalona and P. G. Maropoulos, “A geometrical model for surface roughness prediction when face milling Al 7075-T7351 with square insert tools,” *Journal of Manufacturing Systems,* vol. 36, pp. 216-223, 2015.

[46] Y. Feng, T. P. Hung, Y. T. Lu, Y. F. Lin, F. C. Hsu, C. F. Lin, Y. C. Lu, X. Lu and S. Y. Liang, “Surface roughness modeling in Laser-assisted End Milling of Inconel 718,” *Machining Science and Technology,* vol. 23, no. 4, pp. 650-668, 2019.

[47] Y. Feng, F. C. Hsu, Y. T. Lu, Y. F. Lin, C. T. Lin, C. F. Lin, Y. C. Lu, X. Lu and S. Y. Liang, “Surface roughness prediction in ultrasonic vibration-assisted milling.,” *Journal of Advanced Mechanical Design, Systems, and Manufacturing*, vol. 14, no. 4, pp. JAMDSM0063-JAMDSM0063, 2020.

[48] K. F. Ehmann and M. S. Hong, “A generalized model of the surface generation process in metal cutting,” *CIRP Annals,* vol. 43, no. 1, pp. 483-486, 1994.

[49] M. Arizmendi, F. J. Campa, J. Fernández, L. N. Lopez de Lacalle, A. Gil, E. Bilbao, F. Veiga and A. Lamikiz, “Model for surface topography prediction in peripheral milling considering tool vibration,” *CIRP Annals,* vol. 58, no. 1, pp. 93-96, 2009.

[50] C. Zhang, S. Guo, H. Zhang and L. Zhou, “Modeling and predicting for surface topography considering tool wear in milling process,” *The International Journal of Advanced Manufacturing Technology,* vol. 68, no. 9, pp. 2849-2860, 2013.

[51] M. Arizmendi, J. Fernández, L. N. Lopez de Lacalle, A. Lamikiz, A. Gil, J. A. Sánchez, F. J. Campa and F. Veiga, “Model development for the prediction of surface topography generated by ball-end mills taking into account the tool parallel axis offset. Experimental validation,” *CIRP Annals,* vol. 57, no. 1, pp. 101-104, 2008.

[52] S. H. Ryu, D. K. Choi and C. N. Chu, “Roughness and texture generation on end milled surfaces,” *International Journal of Machine Tools and Manufacture,* vol. 46, no. 3, pp. 404-412, 2006.

[53] P. Franco, M. Estrems and F. Faura, “A study of back cutting surface finish from tool errors and machine tool deviations during face milling,” *International Journal of Machine Tools and Manufacture,* vol. 48, no. 1, pp. 112-123, 2008.

[54] I. Buj-Corral, J. Vivancos-Calvet and H. Gonzalez-Rojas, “Influence of feed, eccentricity and helix angle on topography obtained in side milling processes,” *International Journal of Machine Tools and Manufacture,* vol. 51, no. 12, pp. 889-897, 2011.

[55] S. Zhenyu, L. Luning and L. Zhanqiang, “ Influence of dynamic effects on surface roughness for face milling process.,” *The International Journal of Advanced Manufacturing Technology,* vol. 80, no. 9, pp. 1823-1831, 2015.

[56] S. Wojciechowski, P. Twardowski, M. Pelic, R. W. Maruda, S. Barrans and G. M. Krolczyk, “Precision surface characterization for finish cylindrical milling with dynamic tool displacements model,” *Precision Engineering,* vol. 46, pp. 158-165, 2016.

[57] O. E. E. K. Omar, T. El-Wardany, E. Ng and M. A. Elbestawi, “An improved cutting force and surface topography prediction model in end milling,” *International Journal of Machine Tools and Manufacture,* vol. 47, no. 7, pp. 1263-1275, 2007.

[58] X. Lu, X. Hu, Z. Jia, M. Liu, S. Gao, C. Qu and S. Y. Liang, “Model for the prediction of 3D surface topography and surface roughness in micro-milling Inconel 718,” *The International Journal of Advanced Manufacturing Technology,* vol. 94, no. 5, pp. 2043-2056, 2018.

[59] X. Lu, H. Zhang, Z. Jia, Y. Feng and S. Y. Liang, “Floor surface roughness model considering tool vibration in the process of micro-milling,” *The International Journal of Advanced Manufacturing Technology,* vol. 94, no. 9, pp. 4415-4425, 2018.

[60] G. Urbikain and L. N. Lopez de Lacalle, “Modelling of surface roughness in inclined milling operations with circle-segment end mills,” *Simulation Modelling Practice and Theory,* vol. 84, pp. 161-176, 2018.

[61] S. Shimada, N. Ikawa, H. Tanaka, G. Ohmori, J. Uchikoshi and H. Yoshinaga, “Feasibility study on ultimate accuracy in microcutting using molecular dynamics simulation,” *CIRP annals,* vol. 42, no. 1, pp. 91-94, 1993.

[62] S. K. Pattnaik, N. K. Bhoi, S. Padhi and S. K. Sarangi, “Dry machining of aluminum for proper selection of cutting tool: tool performance and tool wear.,” *The International Journal of Advanced Manufacturing Technology,* vol. 98, no. 1, pp. 55-65, 2018.

Appendix

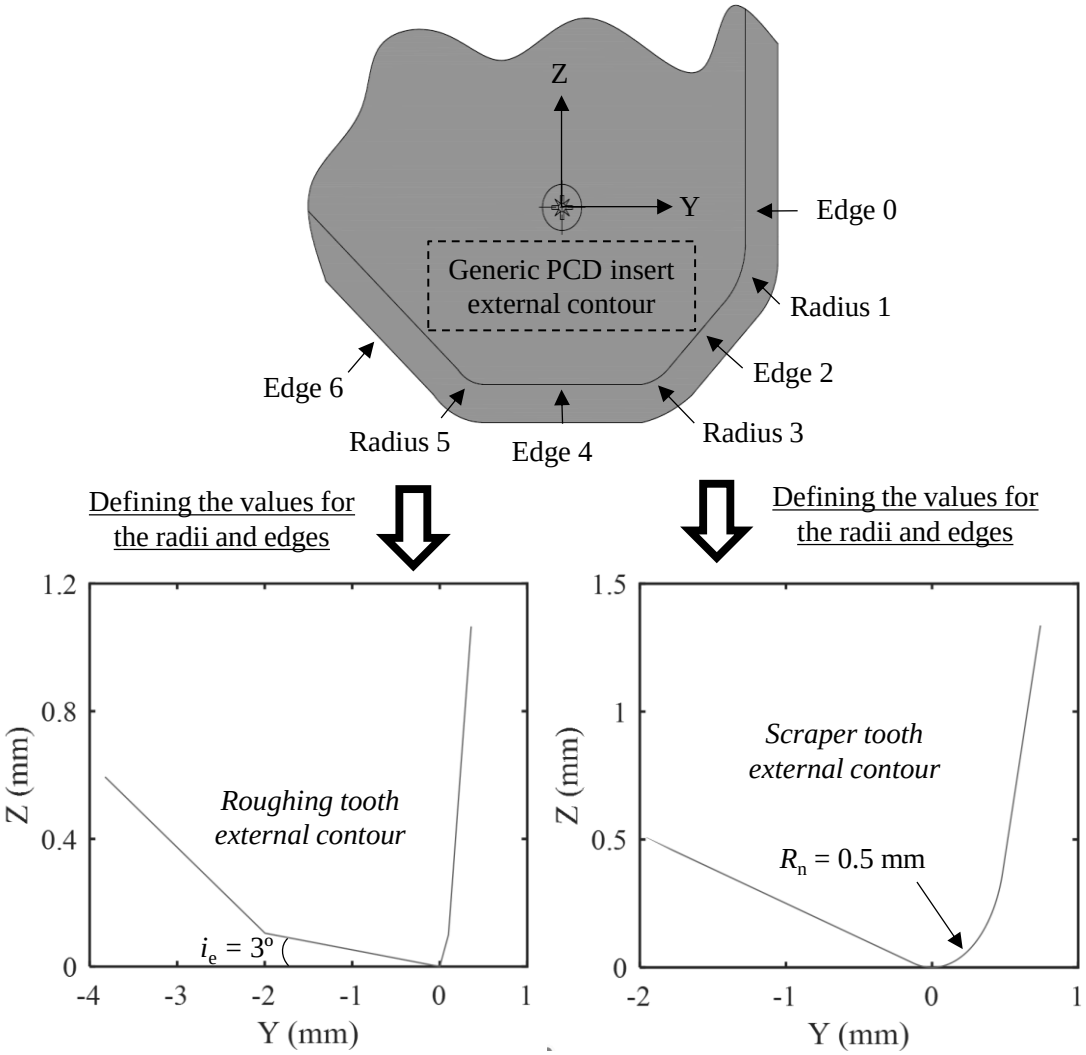

Figure 31. Schematic representation of the external contour of a generic insert. Roughing and scraper teeth geometries are generated by defining values to each radii and edges of the generic insert.

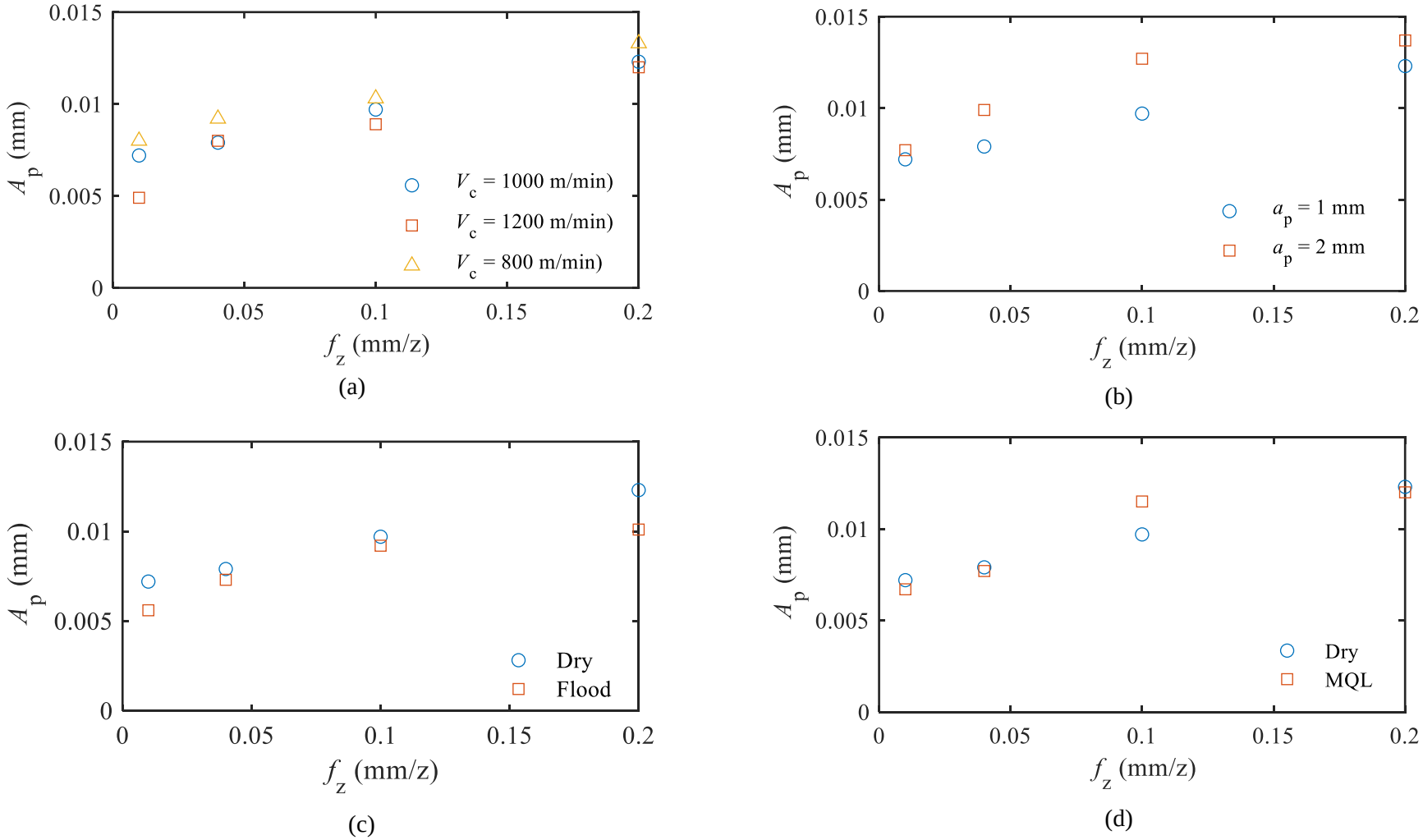

Figure 32. Influence of cutting conditions over the amplitude of the high-pass filtered profiles: a) cutting speed, b) depth of cut, c) lubricant (flood), and d) lubricant (MQL). The analysis is performed for different feed rates.

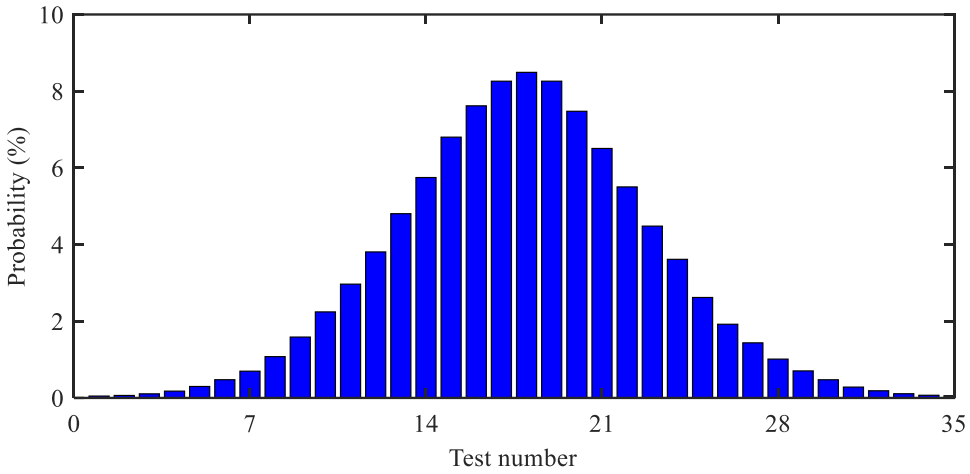

Figure 33. Probabilities of appearance of the peaks and valleys of each high-pass filtered profile. Peaks and valleys were classified into 35 groups depending on their values.

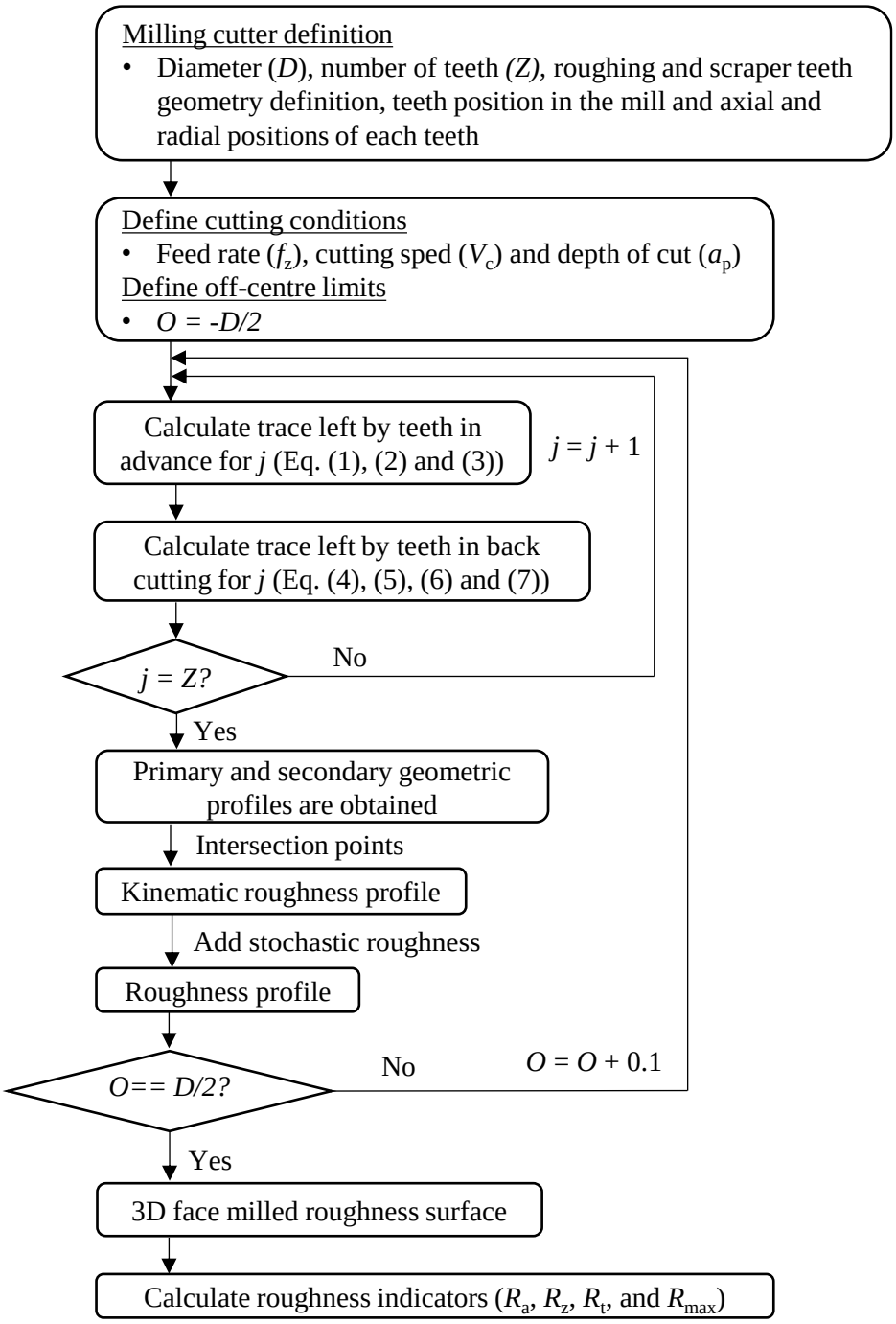

Figure 34. Flow chart for the modelling of the roughness. After defining the cutter geometry and the cutting conditions, the trace left by each tooth is calculated. With the traces, the primary and secondary geometric profiles are obtained, with which the kinematic roughness profile is achieved. Adding the stochastic roughness, the roughness profile is generated. The process is repeated for the complete width of cut to obtain a 3D face milled roughness surface. Finally, roughness indicators are calculated.

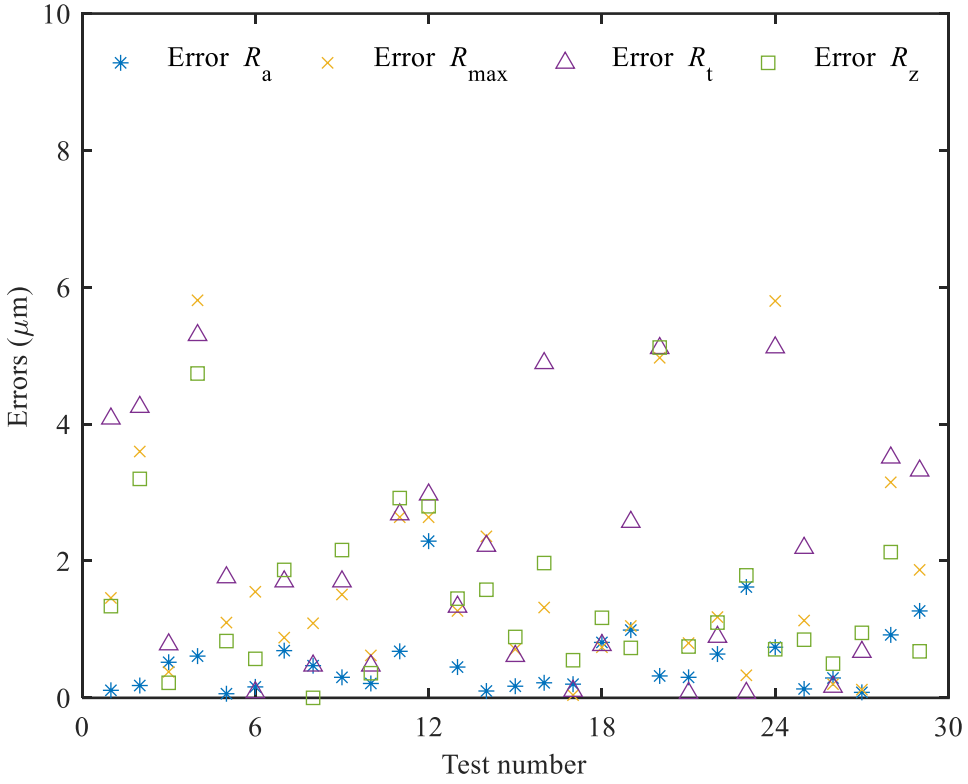

Figure 35. Errors between experimental and modelled roughness indicators at O = 0 mm for each of the 29 tested cutting conditions. The cutting conditions of each test number are detailed in Table 3.

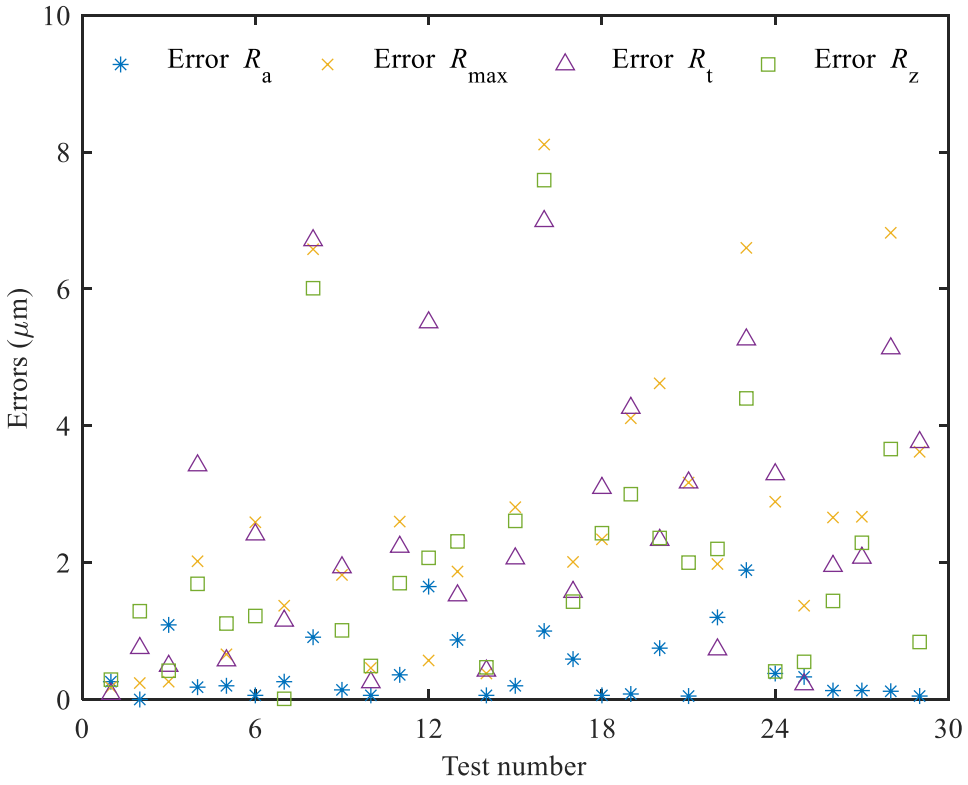

Figure 36. Errors between experimental and modelled roughness indicators at O = 10 mm for each of the 29 tested cutting conditions. The cutting conditions of each test are detailed in Table 3.

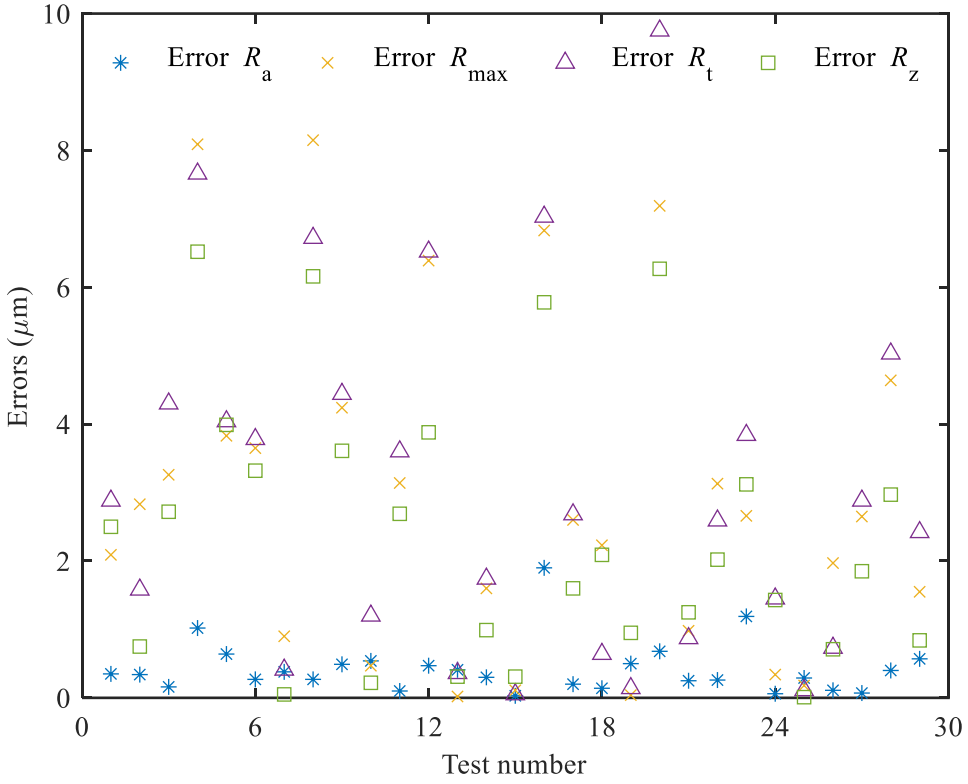

Figure 37. Errors between experimental and modelled roughness indicators at O = 20 mm for each of the 29 tested cutting conditions. The cutting conditions of each test are detailed in Table 3.